Measurement of neutrino interactions with a production of three charged pions in the final state in the MicroBooNE

Tusharadri Mahmud

MSc by Research - Physics

Supervisor

Prof. Jaroslaw Nowak

Lancaster University

Department of Physics

March 2025

Abstract

This dissertation presents a study of muon neutrino (ν_μ) interactions in the MicroBooNE experiment that produce a muon and three charged pions ($3\pi^+$), along with other non-muon, non-pion particles. Using MicroBooNE's liquid argon time projection chamber (LArTPC) at Fermilab, a comprehensive selection strategy is developed to isolate this complex final state. Both inclusive and specialised selections are implemented, with a focus on incorporating a boosted decision tree (BDT) to enhance background rejection while maintaining signal integrity.

Comparative selection cuts analyses for both NuMI and BNB beam configurations show that BDT-based selections significantly improve purity in the final selection cut tables. Though signal efficiency decreases, particularly after the three charged pion cut, the selected events are cleaner and better suited for precision studies. An investigation into the efficiency drop associated with the three pion cut reveals that pion reconstruction especially momentum, track score and proximity to the interaction vertex plays a critical role. This work improves multi-pion event selection in LArTPCs and provides a solid foundation for future analyses of complex neutrino interactions in MicroBooNE and other similar experiments.

Acknowledgements

Over the course of this journey, I have been fortunate to receive support, guidance and encouragement from many incredible individuals. I am deeply grateful to all who have played a part in shaping my academic and personal growth during this time.

First and foremost, I would like to express my sincerest gratitude to my supervisor, Jarek Nowak, whose kindness, wisdom and unwavering support have meant the world to me. Words cannot fully capture how thankful I am for his generosity, both in giving me the opportunity to pursue this course and in guiding me through work that has enriched my understanding of the field. His encouragement and deep knowledge have not only strengthened my confidence but also inspired me to pursue further research. I am forever in debt to him for all he has done.

I would also like to thank Dominic Brailsford for his valuable time, and technical support and for constantly pushing me to engage deeper with my work. To Ishanee Pophale, Isobel Mawby, Niam Patel, Henry Lay and Linhui Gu, I thank them for their constant support, collaborative spirit and for making the learning environment both intellectually stimulating and personally comforting, especially during our time at Fermilab. I am incredibly grateful for all the knowledge and encouragement they have shared with me. A special thanks to Bethany McCusker for providing me with essential resources at the beginning of the course.

Alongside the wonderful people at Lancaster, I would also like to express my appreciation for the members of the MicroBooNE collaboration. In particular, Chris Thorpe for his time, support and technical help, Patrick Green for his advice and encouragement. Diego Andrade and Jennifer Tyler for their support during my Fermilab visit. To everyone who has contributed to my academic journey - thank you. Your kindness and wisdom have made a lasting impact on me.

Contents

List of Tables

List of Figures

1 Introduction

Neutrinos are among the most elusive particles in the Standard Model, interacting only via the weak force, which makes their detection particularly challenging. Despite their evasiveness, neutrinos play a crucial role in understanding fundamental physics, including neutrino oscillations and the underlying processes governing their interactions with matter. The MicroBooNE experiment, a liquid argon time projection chamber (LArTPC) located at Fermilab, is designed to investigate neutrino interactions with high precision[10]. This dissertation focuses on the measurement of muon neutrino (ν_μ) interactions that produce a final state containing a muon (μ), three charged pions($3\pi^+$) and any additional particles that are neither muons nor pions, using data from the MicroBooNE experiment. The primary focus of this work is to develop a comprehensive selection strategy to isolate and analyse the signal definition effectively. A significant portion of the research is dedicated to detailing the methodology behind the selection process, including the inclusive selection to capture a broad spectrum of relevant interactions and a more specialised selection aimed specifically at identifying events with three charged pions. These selections are constructed and optimised using various software techniques integral to the MicroBooNE experiment, ensuring precise event reconstruction and classification. Furthermore, this research extends beyond simple event identification by conducting a detailed analysis of the pion kinematics. In addition, two distinct beam configurations are studied. By systematically evaluating the event selection criteria and the resulting pion distributions, this work provides valuable insights into the dynamics of multi-pion production, contributing to a more refined understanding of the MicroBooNE dataset and its implications for future analyses. The findings from this study not only enhance the accuracy of multi-pion event reconstruction but also offer a foundation for further investigations into similar interaction channels in liquid argon time projection chambers.

Alongside the main analysis, I contributed to a service task for the MicroBooNE production team during my course, which significantly enhanced my understanding of the experimental framework and data handling processes. This hands-on involvement in production work provided practical insights into the infrastructure behind data collection and processing. I also had the opportunity to visit Fermilab, where I experienced

the collaborative environment of a large-scale international experiment firsthand, deepening my appreciation for teamwork and interdisciplinary communication in particle physics.

1.1 The Standard Model

The Standard Model (SM) of particle physics is a critical framework that describes the fundamental building blocks of nature and the forces governing their interactions. The model categorises all known elementary particles into two main classes: fermions and bosons. Fermions, which include quarks and leptons, form the matter we observe, while bosons mediate the forces between them. The six quarks -up, down, charm, strange, top and bottom along with the six leptons - electron, muon, tau and their associated neutrinos are arranged into three generations. Each generation shares similar properties but differs in mass. The SM explains three of the four fundamental forces: the electromagnetic force, mediated by photons (γ); the strong force, mediated by gluons (g); and the weak force, mediated by ($W^{\pm}$) and (Z^0) bosons. The weak force is especially important for neutrinos, as they mainly interact through it[11][12]. As seen in Figure 1, the Higgs boson, discovered in 2012 at the Large Hadron Collider (LHC), provides an explanation for how particles acquire mass through interactions with the Higgs field[13][1].

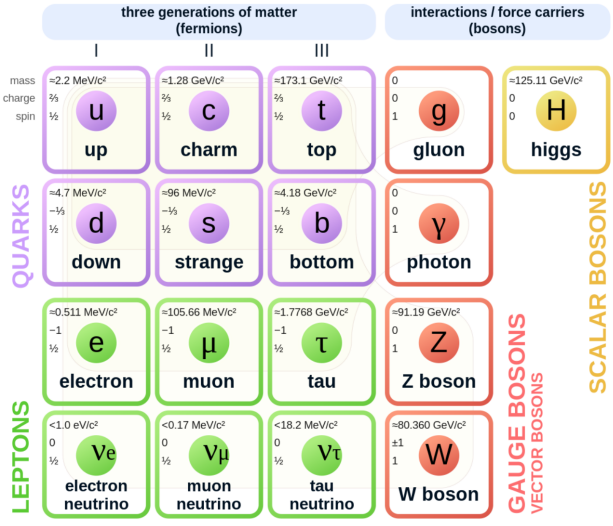

Figure 1: The Standard Model [1]

While the Standard Model has been incredibly successful in explaining particle interactions, it faces significant limitations, particularly in relation to neutrinos. The most glaring of these limitations is the original assumption of the model that neutrinos are massless[14][15]. This was contradicted by the discovery of neutrino oscillations, a phenomenon in which neutrinos switch between different types (flavours) as they propagate. This behaviour directly implies that neutrinos must have mass, which the Standard Model could not predict. As a result, the model requires modification to account for this newly discovered property of neutrinos[15][16].

Furthermore, the SM does not fully explain why neutrino masses are so small compared to other elementary particles, nor does it provide a mechanism for the oscillation patterns observed experimentally. The weak interactions described by the SM are not sufficient to explain these phenomena, suggesting the existence of new physics beyond the model. Additionally, the model's treatment of neutrinos does not account for the intricate mixing of neutrino flavours, which remains an open question in neutrino physics[16]. Beyond neutrinos, the Standard Model also fails to explain several other crucial phenomena. It does not incorporate gravity and its hypothesised force-carrying particle for gravity, graviton[17]. Furthermore, SM accounts for only a small fraction of the matter in the universe. Most of the universe's mass is made up of dark matter, which the Standard Model fails to describe and dark energy, which is thought to drive the accelerated expansion of the universe, remains unexplained[14]. The SM also does not address the matter-antimatter asymmetry, where there is more matter than antimatter in the universe. These limitations point to the need for a more unified theory that extends beyond the Standard Model, incorporating the missing pieces of the universe[14][18].

1.2 Neutrinos

The study of neutrinos has progressed from theoretical predictions to advanced experimental research. Wolfgang Pauli first postulated neutrinos to explain missing energy in beta decay and their existence was confirmed by Clyde Cowan and Frederick Reines[19][20]. The Homestake Experiment was the first to detect solar neutrinos, laying the foundation for investigation into their properties[21]. The Super-Kamiokande

experiment and the Sudbury Neutrino Observatory (SNO) were key in confirming that neutrinos oscillate between different types, resolving the solar neutrino problem[22]. Prior to these discoveries, experiments observed fewer solar neutrinos than expected. Super-Kamiokande demonstrated that atmospheric neutrinos change flavour as they travel, while SNO detected all three neutrino flavours, showing that solar neutrinos were oscillating into previously undetectable types. This confirmed that neutrinos have mass, overturning the previous belief that they were massless and reshaping our understanding of particle physics[22][23]. Subsequent experiments such as Hyper-Kamiokande will continue to refine our knowledge of neutrino oscillations, studying the differences in neutrino and antineutrino behaviour. Meanwhile, the development of liquid argon time projection chambers (LArTPCs) has led to new experimental capabilities[24]. ArgoNeuT and MicroBooNE demonstrated the high-resolution measurement of neutrino interactions, allowing for more precise cross-section measurements. These advances paved the way for the Short Baseline Neutrino Program (SBN), including ICARUS and SBND, which focus on neutrino oscillations and the search for sterile neutrinos[25]. ProtoDUNE demonstrated the scalability of LArTPC technology, setting the stage for the Deep Underground Neutrino Experiment (DUNE), which will utilise a large-scale detector to study neutrinos in greater detail, addressing questions about neutrino mass and potentially revealing new physics beyond the Standard Model[26].

1.2.1 Interactions

Neutrino interactions are divided into two major categories based on the mediator of the interaction and the resulting final state: charged-current (CC) and neutral-current (NC) processes[27]. Each category exhibits distinct characteristics and plays a complementary role in our understanding of neutrino behaviour. In charged current interactions, the neutrino exchanges a W boson with a target nucleon, thereby converting it into its corresponding charged lepton. This flavour-changing process is central to the identification of neutrino species in experimental analyses, since the appearance of a charged lepton (such as a muon or electron) provides an unambiguous signature of the interaction.

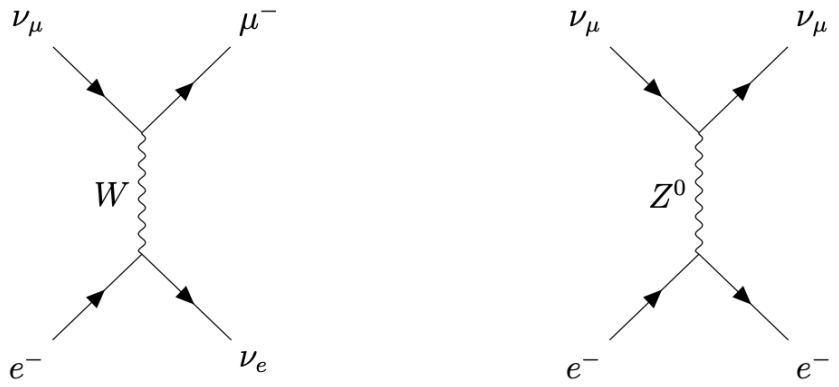

Figure 2: Feynman diagram of:(CC) interaction(left) and (NC) interaction(right).

The generic CC process is represented by

$$\nu_l + N \rightarrow l^- + X \tag{1}$$

where ν_l denotes a neutrino of flavour (such as ν_μ denotes the muon neutrino flavour), N is the target nucleon and X symbolises the resulting hadronic state which may include nucleons, mesons and other secondary particles. The charged lepton produced in such interactions acts as a "tag" that not only identifies the neutrino flavour but also facilitates energy reconstruction; an essential parameter in neutrino oscillation research[27].

Understanding the difference between interactions on free versus bound nucleons, as well as the influence of final state interactions (FSI), is crucial for precise event reconstruction in liquid argon time projection chambers (LArTPCs) like MicroBooNE[28]. When neutrinos interact with free nucleons, such as those in hydrogen targets (e.g. protium), the process is straightforward. The nucleon, unaffected by nuclear forces, directly receives energy and momentum from the neutrino, leading to a predictable outcome. For instance, in a charged current quasi-elastic interaction with a free neutron, a muon neutrino transforms into a muon, while the neutron converts into a proton. The analysis of these interactions becomes less complicated when nuclear effects such as binding energy and Fermi motion are absent. In contrast, interactions with nucleons bound within a nucleus, such as argon, introduce complexities. Bound nucleons possess intrinsic momentum (Fermi motion) even before interaction, smearing the energy

and angular distributions of outgoing particles. Additionally, binding energy alters interaction dynamics, while Pauli blocking restricts final states, reducing the observable cross-section[29][30]. Once a neutrino interacts within a nucleus, the resulting particles, charged leptons, nucleons, or mesons, must traverse the nuclear medium before detection. This stage, known as final-state interactions (FSI), significantly alters the observed event[30]. In dense environments like liquid argon, outgoing particles may undergo elastic or inelastic scattering, charge exchange, or absorption. For example, a pion produced in a resonant interaction might lose energy or change charge upon colliding with nucleons, while a recoil nucleon can scatter and modify its trajectory[31][29]. FSI plays a crucial role in experiments like MicroBooNE, where nuclear effects distort particle motion, complicating the reconstruction of neutrino energy and interaction type.

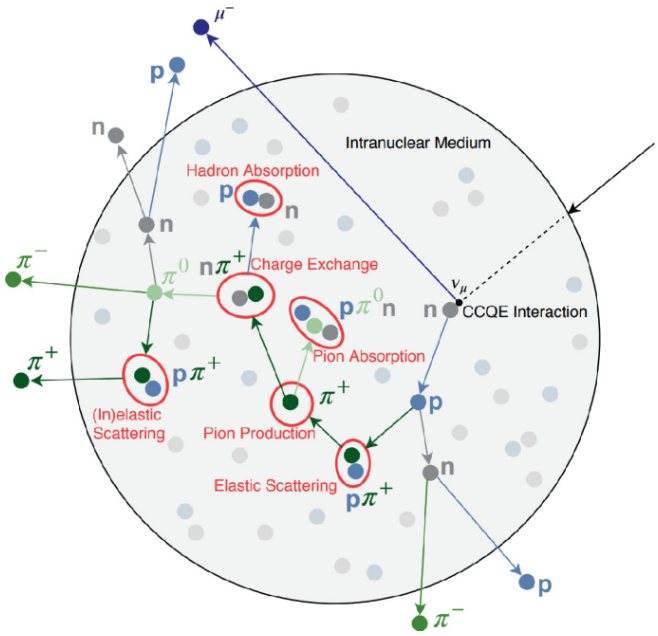

Figure 3: Various potential final state interaction (FSI) processes[2].

CC interactions are further sub-categorised into three principal regimes, determined by the incident neutrino energy and the kinematics of the interaction: quasi-elastic (QE) scattering, resonant (RES) scattering and deep-inelastic scattering (DIS)[32][33].

At low neutrino energies, typically from a few hundred MeV to a few GeV, the main interaction process is quasi-elastic (QE) scattering. In this type of interaction, a neutrino

collides with a nucleon, usually a neutron, inside the nucleus. The neutrino exchanges a W boson, producing a charged lepton and a recoiling nucleon without exciting it to a higher energy state. For example, when a muon neutrino interacts with a neutron, it produces a muon and a proton:

$$\nu_\mu + n \rightarrow \mu^- + p \tag{2}$$

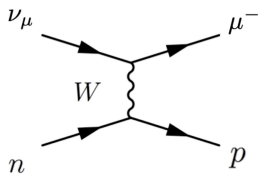

Figure 4: Feynman Diagram of quasi-elastic (QE) scattering. [3]

This process involves relatively simple motion, as the nucleon remains mostly unchanged, only switching between a neutron and a proton. Because of this, quasi-elastic interactions are highly useful in neutrino oscillation experiments. The simplicity of the final particles allows one to accurately determine the neutrino's energy by measuring the motion of the charged lepton and nucleon. In nuclei like argon, nuclear effects such as final state interactions (FSI) and nucleon correlations take effect, making energy calculations more complex.

As the neutrino energy increases to a few GeV, resonant scattering becomes increasingly prominent. In resonant interactions, the neutrino has sufficient energy to excite the target nucleon into a higher-energy resonant state (most notably the Delta (Δ) resonance), which then decays into a nucleon and one or more pions. A representative resonant interaction is:

$$\nu_\mu + n \rightarrow \mu^- + \Delta^+ \tag{3}$$

where

$$\Delta^+ \rightarrow p + \pi^0 \tag{4}$$

$$\Delta^+ \rightarrow n + \pi^+ \tag{5}$$

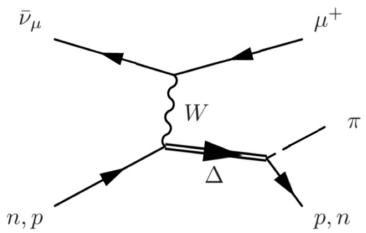

Figure 5: Feynman Diagram of Resonant Interaction[3]

In these events, the appearance of pions in the final state offers additional handles for probing the internal structure of the nucleon and the dynamics of hadronic excitation. The resonance peak observed in the interaction cross-section is a distinctive feature that aids experimental separation of resonant processes from other types of interactions. In experiments utilising liquid argon detectors, such as MicroBooNE, resonant scattering is particularly important because it contributes to the signal definition involving charged pion production[28][34]. For instance, the interaction:

$$\nu_\mu + Ar \rightarrow \mu^- + \pi^+ + X \tag{6}$$

where X represents any additional nuclear debris, is a resonant CC process that directly contributes to the measured signal and helps in constraining models of nucleon resonance production and decay.

At neutrino energies above 10 GeV, deep-inelastic scattering (DIS) becomes the dominant interaction. In this process, the neutrino interacts directly with the quarks inside a nucleon rather than with the nucleon as a whole. A high-energy W boson mediates the interaction, breaking apart the nucleon and producing a complex mix of hadrons[33][35]. The general form of a DIS interaction is:

$$\nu_l + N \rightarrow l^- + X \tag{7}$$

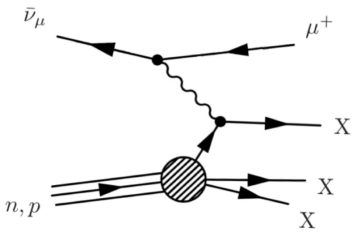

Figure 6: Feynman Diagram of Deep Elastic Scattering[3]

where N represents the target nucleon, l^- is the outgoing lepton and X consists of multiple hadrons, such as pions, kaons and other particles formed from the struck quark. DIS interactions provide valuable information about the inner structure of nucleons by probing quark and gluon dynamics at high energies. Since the cross-section increases rapidly with energy, DIS plays a crucial role in high-energy neutrino experiments. Although less common in lower-energy detectors like MicroBooNE, it helps refine parton distribution functions (PDFs) and improves our understanding of strong interactions in the electroweak sector. [19]

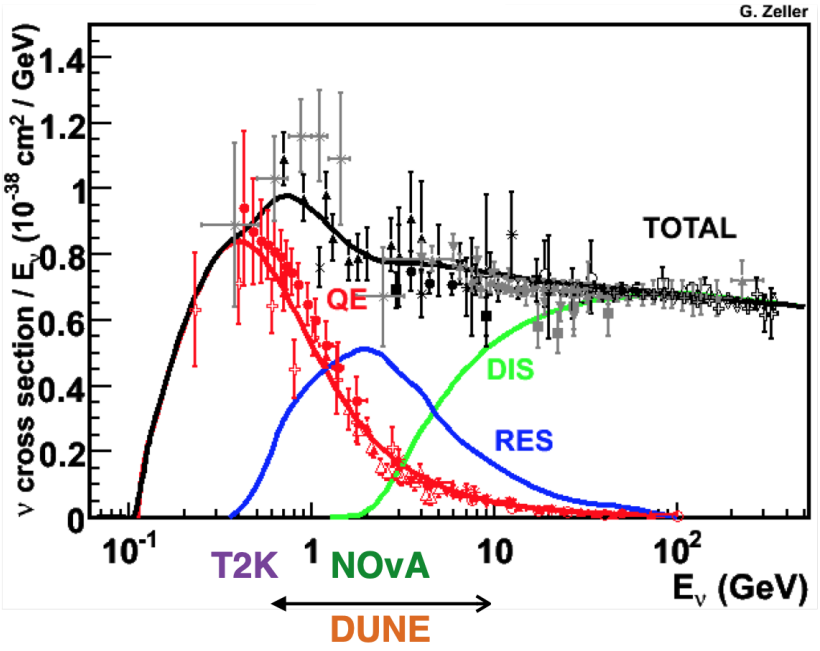

Figure 7: 'Current measurements of CC neutrino and antineutrino cross sections in intermediate energy range', from the follwoing paper[4]

In contrast to CC interactions, neutral current (NC) interactions occur via the exchange of a Z boson[36]. In NC processes, the neutrino retains its flavour as it scatters

off a nucleon and no charged lepton is produced:

$$\nu_l + N \rightarrow \nu_l + X \tag{8}$$

The resulting hadronic system X exhibit signs of nuclear excitation or particle production, such as the emission of nucleons or pions. NC interactions, though less directly useful for signal definition in flavour-specific analyses, are crucial for understanding background processes. The NC contribution, particularly via the production of neutral pions, is carefully modeled and subtracted to ensure the purity of the CC signal in neutrino oscillation studies[33][36].

1.2.2 Oscillations

Neutrino oscillations are crucial to modern particle physics because they offer insights into neutrino mass and any phenomena beyond the Standard Model. Neutrinos mix between flavours as they travel. This behaviour arises due to the difference between their flavour states and mass eigenstates. Therefore, precise modeling of neutrino interactions is necessary, as any uncertainty in interaction cross-sections can skew the measurement of oscillation parameters. In this research, the focus is on a distinct interaction: a muon neutrino interacting with a liquid argon nucleus, resulting in a final-state muon and three charged pions. This interaction is particularly important for long-baseline oscillation experiments. Understanding these interactions is vital for long-baseline oscillation experiments, where misidentifying interaction modes can lead to inaccuracies in reconstructing key oscillation parameters, such as neutrino mixing angles and mass-squared differences. The high-resolution capabilities of the MicroBooNE liquid argon time projection chamber (LArTPC) provide detailed data on charged-current pion production interactions[34]. Such interactions serve as essential inputs for reducing systematic errors in large-scale oscillation experiments like DUNE[16].

Neutrino oscillation is a quantum mechanical effect that occurs because the neutrino flavour states ν_e,ν_μ and ν_τ are superpositions of their mass eigenstates ν_1, ν_2 and ν_3[16]. This is expressed mathematically as the following:

$$|\nu_\alpha\rangle = \sum_i U_{\alpha i} |\nu_i\rangle \tag{9}$$

where $|\nu_\alpha\rangle$ represents a neutrino in a given flavour state ($\alpha = e, \mu, \tau$) and $|\nu_i\rangle$ are the mass eigenstates with definite masses m_i and $U_{\alpha i}$ is an element of the Pontecorvo-Maki-Nakagawa-Sakata (PMNS) matrix, which describes the mixing between flavour and mass states.

The PMNS matrix can be illustrated using three distinct mixing angles, θ_{12}, θ_{23} and θ_{13} and a single complex phase δ, commonly exhibited as the following:

$$U_{PMNS} = \begin{pmatrix} U_{e1} & U_{e2} & U_{e3} \\ U_{\nu_1} & U_{\nu_2} & U_{\nu_3} \\ U_{\tau_1} & U_{\tau_2} & U_{\tau_3} \end{pmatrix} = \begin{pmatrix} 1 & 0 & 0 \\ 0 & c_{23} & s_{23} \\ 0 & -s_{23} & c_{23} \end{pmatrix} \begin{pmatrix} c_{13} & 0 & s_{13}e^{-i\delta} \\ 0 & 1 & 0 \\ s_{13}e^{i\delta} & 0 & c_{13} \end{pmatrix} \begin{pmatrix} c_{12} & s_{12} & 0 \\ -s_{12} & c_{12} & 0 \\ 0 & 0 & 1 \end{pmatrix} \tag{10}$$

where $c_{ij} = cos\theta_{ij}$ and $s_{ij} = sin\theta_{ij}$ represent the mixing angles[33][16].

δ is the CP-violating phase, which affects differences between neutrino and antineutrino oscillations[33].

As neutrinos propagate, their mass eigenstates acquire different phase factors due to their different masses. The probability of a neutrino initially in the flavour state ν_α being detected as ν_β after traveling a distance L is given by:

$$P_{\nu_\alpha \to \nu_\beta}(L) = \left| \sum_j U_{\beta j} U^*_{\alpha j} \exp\left(-i \frac{\Delta m^2_{j1} L}{2E} \right) \right|^2 \tag{11}$$

where Δm^2_{j1} is the squared mass difference between mass eigenstates, L is the distance traveled by the neutrino, $U_{\beta j} U^*_{\alpha j}$ are the elements of the PMNS matrix and E is the neutrino energy[33].

Neutrino oscillations are significant because they hold the possibility to show a difference in behavior between neutrinos and antineutrinos, this is known as CP violation. This difference could help explain why our universe has more matter than antimatter[37]. CP violation happens when the probability of a neutrino changing type is not the same as for an antineutrino:

$$P(\nu_\alpha \to \nu_\beta) \neq P(\overline{\nu}_\alpha \to \overline{\nu}_\beta) \tag{12}$$

This effect comes from a complex phase in the PMNS matrix. If CP violation in neutrinos is confirmed, it could be a hint towards the process that caused a matter-dominated universe seen today[37]. Another important motive in neutrino oscillation research is to understand the mass hierarchy; whether the three neutrino masses follow a normal order ($m_1 < m_2 < m_3$) or an inverted one ($m_3 < m_1 < m_2$). Knowing this is key to understanding how neutrinos get their mass[38]. In addition neutrino experiments are also conducted for the search for sterile neutrinos, theoretical particles that don't interact through the weak force but could mix with regular neutrinos[39]. Experiments like DUNE, Hyper-Kamiokande and T2HK aim to measure neutrino properties with high precision, focusing on CP violation and mass hierarchy. In order to achieve accurate results, it is important to have understanding of neutrino interactions, especially how neutrinos scatter and interact with other particles.

2 MicroBooNE

The MicroBooNE (Micro Booster Neutrino Experiment) is a liquid argon time projection chamber (LArTPC) neutrino experiment designed to investigate neutrino interactions with high precision. Located at Fermilab National Accelerator Laboratory (FNAL), it is positioned along the Booster Neutrino Beamline (BNB). MicroBooNE plays a key role in studying neutrino oscillations, refining neutrino-argon interaction cross-sections and probing physics beyond the Standard Model. One of its primary objectives is to investigate the low-energy excess of electron-like events previously observed by the MiniBooNE experiment, while also serving as a technological testbed for future large-scale neutrino experiments like DUNE (Deep Underground Neutrino Experiment)[10][24].

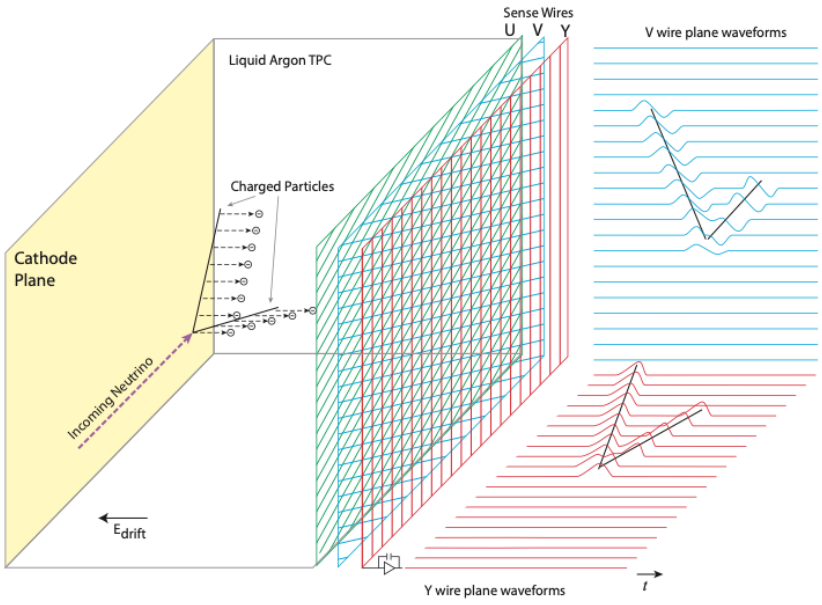

Figure 8: The MicroBooNE LArTPC[5]

MicroBooNE operates as a single-phase LArTPC meaning it operates as both the target medium for interactions and the detection medium for ionisation signals. Holding approximately 170 tons of liquid argon within its detector volume. Liquid argon is an optimal medium for neutrino detection due to its high density, inert nature and cost-effectiveness compared to other noble liquids[40]. To maintain its liquid state and ensure high purity levels, the argon is kept at a temperature of 87 Kelvin (K). The

core detection principle of the experiment relies on ionisation electrons produced when neutrinos interact with argon nuclei. These electrons drift across the TPC volume, which measures $2.3 \times 2.6 \times 10.4$ (m^3) and are recorded by a series of anode wire planes for precise event reconstruction[5][24].

The TPC consists of three essential components: a cathode plane at one end, a field cage surrounding the drift region and three anode wire planes at the opposite end. The cathode plane is powered to establish a uniform drift electric field of 273 V/cm, which guides ionisation electrons toward the anode. The field cage minimises divergence of the drift electrons from their intended trajectory, ensuring they reach the anode wire planes accurately. These anode planes, each separated by 3 cm, consist of fine conducting wires spaced a few millimetres apart. In a detector with N anode wire planes, the inner N-1 serve as induction planes at a lower potential, allowing electrons to pass through them, while the outermost plane collects the final signals. By utilising wire planes with different orientations, two-dimensional event reconstruction is achieved, while the third dimension is determined by the drift time of the electrons[41][24].

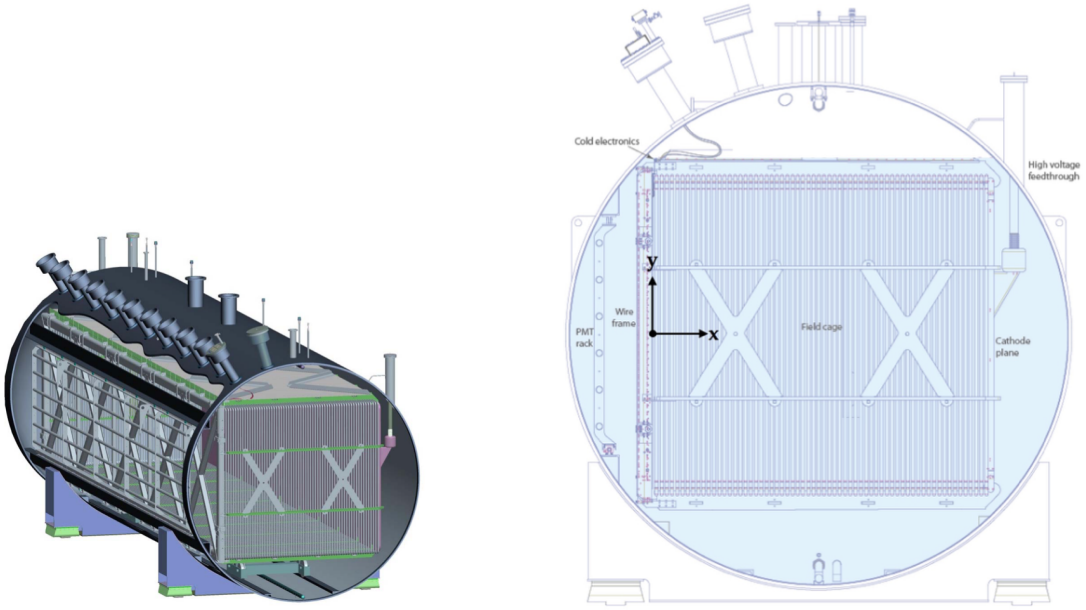

Figure 9: Schematic diagram of the MicroBooNE LArTPC, showing its arrangement inside the cryostat (left) and a cross-sectional view of the detector (right)[5].

To improve time resolution and neutrino event detection, MicroBooNE is also equipped with a system of 32 photomultiplier tubes (PMTs). These PMTs detect the scintillation light emitted when charged particles traverse the liquid argon, providing a precise timing reference that is crucial for identifying neutrino interactions. In addition, this timing system helps reject cosmic ray backgrounds, which are a significant challenge for MicroBooNE since it is located on the surface rather than underground. Cosmic rays produce long tracks from muons that can mimic neutrino interactions and their presence also induces a space-charge effect, causing slight distortions in the electric field within the TPC[6][42].

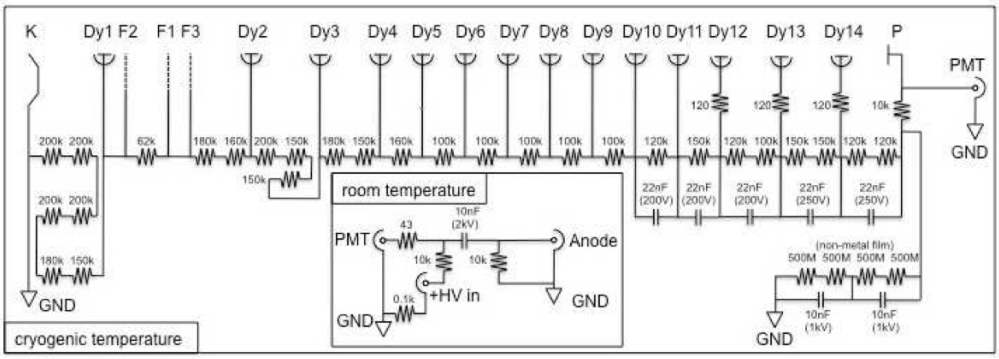

Figure 10: The MicroBooNE PMT[6].

The Booster Neutrino Beam (BNB) at Fermilab is a high-intensity, predominantly muon neutrino (ν_μ) beam. The beam is produced by accelerating protons to an energy of 8 GeV using the Fermilab Booster synchrotron. These high-energy protons are then directed onto a solid beryllium target, where they undergo strong interactions, generating an array of secondary particles, primarily charged pions (π^+ and π^-) and kaons (K^+ and K^-). These mesons are subsequently focused using a system of magnetic horns before being allowed to travel down a decay pipe. During this transit, the charged pions and kaons decay into muons and neutrinos, leading to the production of a predominantly muon neutrino beam. The BNB design ensures that the vast majority of neutrinos originate from pion decays $\pi^+ \to \mu^+ + \nu_\mu$, though a smaller fraction arises from kaon and muon decays, which introduce both electron neutrinos (ν_e) and anti-neutrinos into the beam. Since MicroBooNE is positioned approximately 470 meters from the target, it samples these neutrinos as they pass through its liquid argon time projection chamber (LArTPC)[43].

The Neutrinos at the Main Injector (NuMI) beam at Fermilab serves as a second high-intensity neutrino source for the MicroBooNE experiment, complementing the primary Booster Neutrino Beam (BNB). Unlike the BNB, which is optimised for short-baseline neutrino experiments and has a peak energy around 800 MeV, the NuMI beam is designed for long-baseline neutrino oscillation studies and operates at significantly higher energies, reaching several GeV. This higher-energy neutrino source allows MicroBooNE to explore neutrino interactions in a different energy regime. The NuMI beam is produced by directing 120 GeV protons from Fermilab's Main Injector onto a thick graphite target. When these high-energy protons collide with the target, they generate secondary mesons, primarily charged pions (π^+ and π^-) and kaons (K^+ and K^-), which are then focused by a system of magnetic horns[44]. The focusing system plays a crucial role in determining the neutrino beam composition, as it selectively enhances the charge-sign of mesons, thus controlling whether the beam is dominated by neutrinos or anti-neutrinos. These mesons subsequently travel through a long decay pipe, where they decay in flight, predominantly producing muon neutrinos (ν_μ) along with a smaller fraction of electron neutrinos (ν_e) and their respective anti-neutrinos. As the NuMI beam enters the MicroBooNE detector, neutrinos undergo interactions within the liquid argon target, producing a variety of final-state particles. The higher energy of the NuMI neutrinos increases the likelihood of interactions that go beyond simple quasi-elastic scattering.

While quasi-elastic interactions dominate at lower energies, resonant pion production and deep inelastic scattering become more significant within the NuMI energy range. This enables MicroBooNE to study a wide range of interaction processes, providing crucial data for refining neutrino-argon interaction models[45][46]. The NuMI beam enters the MicroBooNE detector at an 8° off- axis angle compared to the BNB, introducing additional challenges in event reconstruction. While the BNB is aligned nearly perpendicular to the anode wire planes of the TPC, the NuMI beam enters at a steeper angle, requiring corrections to account for differences in track reconstruction efficiency. The angular acceptance of the detector plays a role in determining how well various interaction channels can be studied, as certain interaction topologies may have reduced visibility depending on their orientation relative to the wire planes [44][46].

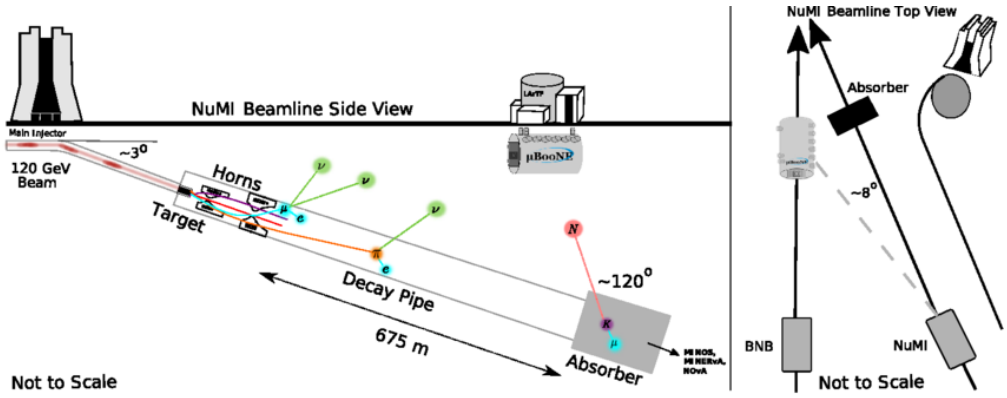

Figure 11: MicroBooNE detecter and the beam targets[7].

Another important process studied by MicroBooNE involves neutral-current interactions that produce neutral pions. These interactions are significant because neutral pions decay into two photons, which can be mistaken for electron neutrino interactions in detectors with lower resolution. MicroBooNE's ability to separate electrons from photons provides valuable insight into this background, improving the reliability of electron neutrino appearance measurements in oscillation experiments[47].

MicroBooNE plays a crucial role in reducing uncertainties in neutrino oscillation measurements by providing precise studies of muon neutrino interactions in argon. Long-baseline experiments rely on accurate neutrino interaction cross-sections to reconstruct oscillation parameters and systematic uncertainties in these cross-sections can bias fundamental measurements such as mixing angles and mass-squared differences. Leveraging high-resolution LArTPC technology, MicroBooNE refines theoretical models advances techniques for future large-scale experiments. Its contributions to oscillation physics, CP violation studies and detector development make it a key component of the broader neutrino research program.

2.1 LArSoft

LArSoft (Liquid Argon Software) is a comprehensive, experiment-agnostic software framework designed to facilitate the simulation, reconstruction and analysis of data from liquid argon time projection chambers (LArTPCs), playing a crucial role in neutrino physics experiments such as MicroBooNE, ICARUS, SBND and DUNE. The unique ca-

pabilities of LArTPCs, which provide millimeter-scale spatial resolution, precise calorimetric measurements and detailed particle tracking, demand advanced computational tools to extract meaningful physics from vast amounts of data. LArSoft, built on Fermilab's art framework (the art framework at Fermilab is a modular C++ software toolkit designed to build, configure and run particle physics data-processing workflows for experiments), provides a unified software environment that ensures consistency across different experiments while allowing custom adaptations for specific detector geometries and data acquisition systems. Given the complexity of neutrino interactions, where multiple final-state particles can emerge and propagate through the detector medium, sophisticated computational frameworks like LArSoft are essential for handling raw detector signals, reconstructing event topologies and providing high-precision measurements of neutrino interaction parameters. The need for such software is amplified by the fact that neutrinos interact weakly with matter, leading to sparse and intricate event signatures that require careful deconvolution of spatial and calorimetric information to achieve reliable interpretations[48].

At its core, LArSoft consists of several key modules that encompass the entire data processing pipeline, beginning with event simulation. The simulation stage models neutrino interactions in liquid argon, accounting for both primary and secondary particle production and their subsequent propagation through the detector. This involves detailed modeling of ionisation processes, charge drift in the detector's electric field, recombination effects and interactions with the readout electronics. Accurate simulations are crucial for comparing experimental data with theoretical expectations, ensuring that systematic uncertainties are well understood and minimised. Following simulation, the raw detector signals undergo signal processing, where noise filtering, deconvolution and waveform shaping techniques are applied to enhance data quality before reconstruction. 'Deconvolution, specifically employs Wiener filtering and Fourier-transform-based techniques to mathematically reverse the detector's response function, mitigating distortions introduced by electronics shaping and induction effects. By transforming signals into the frequency domain, applying optimal filtering methods and converting them back to the time domain, deconvolution enhances charge localisation, reduces noise contributions and refines hit reconstruction, ultimately improving tracking and calorimetric measurements'[48][49]. After signal processing, the next stage involves hit finding and

clustering, where individual ionisation signals (hits) on the detector's readout wires are identified and grouped into clusters representing distinct particle trajectories. The success of this step determines the accuracy of subsequent reconstruction processes. Given that neutrino interactions can produce multiple charged particles traveling in different directions, clustering algorithms must effectively differentiate overlapping signals while maintaining computational efficiency[8].

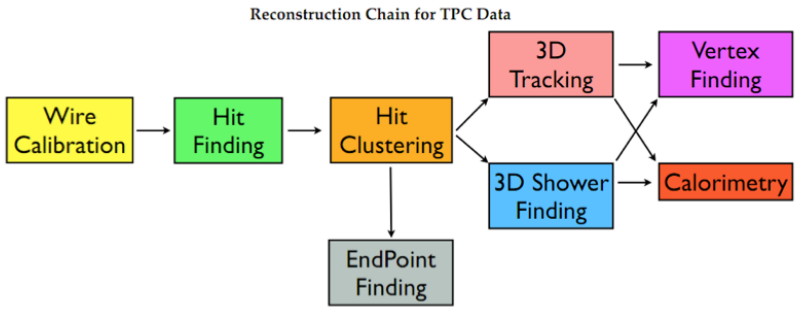

Figure 12: The LArSoft Flowchart[8].

One of LArSoft's most critical components is its 3D reconstruction capability, which converts 2D wire plane projections into fully reconstructed 3D event images. This step is particularly crucial for MicroBooNE, as the experiment relies on high-resolution reconstruction techniques to distinguish between different interaction topologies, such as charged-current quasi-elastic (CCQE) interactions, resonant pion production and deep inelastic scattering events. In traditional neutrino detectors, reconstruction is often hindered by limited spatial resolution, but LArTPCs overcome this by providing detailed images of particle tracks, which LArSoft translates into reconstructed vertices, track angles and particle momenta. The next step in the workflow is particle identification (PID), where reconstructed tracks are classified based on their energy deposition profiles and topological features. This is vital for distinguishing between electrons and photons, a key challenge in MicroBooNE's search for an explanation of the MiniBooNE low-energy excess. Since an excess of electromagnetic-like events could indicate either an unknown neutrino interaction channel or the presence of new physics, accurate PID techniques within LArSoft are essential for drawing robust conclusions from the data. The final major stage is energy reconstruction, where the deposited charge along each track is used to estimate the energies of individual particles. This information is cru-

cial for cross-section measurements, as understanding the energy-dependent behavior of neutrino interactions helps refine theoretical models and improve predictions for next-generation oscillation experiments like DUNE[48].

2.2 Monte Carlo (MC)

Monte Carlo simulations are essential for neutrino experiments like MicroBooNE, allowing researchers to predict neutrino interactions and detector responses based on theoretical models. Since neutrinos interact weakly with matter, direct measurements of all possible interaction types are limited, making simulations necessary to understand how these particles behave. Monte Carlo methods use random sampling techniques to generate neutrino events based on probability distributions that describe cross-sections, final-state particle production and detector effects. This approach enables scientists to reconstruct neutrino energy, analyse systematic uncertainties and compare experimental results with theoretical predictions.

GENIE (Generates Events for Neutrino Interaction Experiments) is the primary Monte Carlo event generator used in MicroBooNE to model neutrino interactions with argon nuclei. It works by simulating neutrino-nucleus collisions using a combination of techniques. When a neutrino enters the detector, GENIE simulates neutrino-nucleus interactions by integrating various theoretical models that describe different energy regimes and interaction processes.̀To model the nuclear environment, it employs the Relativistic Fermi Gas (RFG) model, which assumes that nucleons move freely within a momentum distribution up to the Fermi surface, while more advanced approaches like the Local Fermi Gas (LFG) model account for spatial variations in nucleon density, improving accuracy. For quasielastic (QE) scattering, GENIE incorporates Random Phase Approximation (RPA) corrections to account for nuclear correlations and the Nieves model, which includes multinucleon effects, where a neutrino interacts with a correlated nucleon pair rather than a single nucleon. In resonant pion production, the Rein-Sehgal model describes how a neutrino excites a nucleon into a baryon resonance, which decays by emitting a pion. At higher energies, GENIE utilises Deep Inelastic Scattering (DIS) models, incorporating parton distribution functions (PDFs) to describe neutrino interactions with quarks inside nucleons, leading to multi-particle final states. Additionally,

it includes coherent pion production models, such as Berger-Sehgal, which describe interactions where a neutrino scatters off an entire nucleus, producing a pion without breaking it apart'[50]. Once an interaction occurs, hadron transport models simulate final-state interactions (FSIs), which track how hadrons interact with the surrounding nuclear medium before escaping the nucleus, affecting the observable particles in the detector. By integrating these models, GENIE generates realistic neutrino interaction events, allowing MicroBooNE to compare simulations with experimental data.

After the initial interaction, the resulting particles must be tracked as they move through the MicroBooNE detector, which is where GEANT4 comes into play. GEANT4 is a powerful toolkit used to simulate the passage of particles through matter, taking into account physical processes like ionisation, multiple scattering and energy loss. In MicroBooNE, GEANT4 models how charged particles, such as muons and pions, ionise the liquid argon as they travel, producing free electrons that drift towards the detector's anode wires under an applied electric field. Additionally, GEANT4 simulates the production of scintillation light, which is detected by photomultiplier tubes (PMTs) and used for event timing[51]. The detailed tracking of particles provided by GEANT4 ensures that the detector response is well understood and that background signals, such as cosmic rays, can be distinguished from neutrino interactions.

Once GENIE and GEANT4 have simulated the neutrino interaction and particle propagation, a final step applies realistic detector effects to the simulation. This process accounts for factors such as electronic noise, signal attenuation and distortions in the electric field caused by space-charge effects[42]. These refined simulated events are then processed using the same reconstruction algorithms as real experimental data, allowing for direct comparisons between the two. By adjusting the parameters within GENIE and GEANT4 based on these comparisons, MicroBooNE continuously improves the accuracy of its simulations, ensuring that neutrino interaction models are well-calibrated for precise physics analyses. Monte Carlo generators like GENIE and GEANT4 are essential for neutrino experiments, enabling precise modeling of interactions in liquid argon detectors[50][51].

2.3 Event Reconstruction

Pandora operates as a modular, multi-algorithm framework designed to tackle the complex task of event reconstruction in MicroBooNE's liquid argon time projection chamber (LArTPC). Unlike traditional reconstruction techniques that rely on a single algorithm to interpret detector data, Pandora employs a sophisticated chain of algorithms, each optimised for different stages of the reconstruction process. This approach is particularly crucial for LArTPCs, where neutrino interactions produce detailed, three-dimensional ionisation tracks that must be accurately interpreted to distinguish between different particle types and interaction processes.

The reconstruction process begins with hit formation, where raw charge deposits recorded by the anode wire planes are processed into spatially localised "hits", representing individual energy depositions. Since the LArTPC provides a 2D wire-based projection of the event, these hits must be correctly matched across different wire planes to build a complete 3D representation. Pandora achieves this through 'DBSCAN (Density-Based Spatial Clustering of Applications with Noise)' and 'Sliding Linear Fit' clustering, which group hits into slices—small segments of 'track-like' or 'shower-like' structures that serve as the foundation for higher-level reconstruction[52].

To construct full particle trajectories, Pandora employs a hierarchical pattern recognition approach, incrementally merging and classifying clusters using a large suite of algorithms. 'Projection Matching' and 'Multi-View Pattern Recognition' algorithms ensure accurate 3D reconstruction by aligning clusters across detector views, while 'Principal Component Analysis (PCA) classification' and the 'Radial Distance algorithm' separate track-like patterns, associated with muons, protons, or charged pions, from shower-like structures indicative of electromagnetic cascades. Shower growth and topology-based clustering techniques help refine photon and electron showers by detecting sudden divergences in hit density, ensuring accurate reconstruction. By applying multiple algorithms in sequence—each refining and validating the structures produced by previous steps—Pandora builds an increasingly detailed picture of the event, ensuring robustness against ambiguities such as overlapping tracks or misidentified shower fragments[52].

One of Pandora's most powerful capabilities is cosmic-ray background rejection. This is a critical challenge for MicroBooNE since it operates on the surface, where cosmic muons vastly outnumber neutrino interactions. To mitigate this, Pandora includes dedicated algorithms such as 'Track-Cluster Linking' and 'Timing-Based Cosmic Rejection', which distinguish cosmic-ray tracks from neutrino-induced events by analysing spatial positioning, topology and timing correlations with the beam spill window. By identifying and removing cosmic muons, Pandora enhances the purity of neutrino event samples[53].

Pandora also plays a vital role in final-state particle classification. Once the 'Vertex Association Algorithm' identifies the primary neutrino interaction vertex, Pandora analyses the outgoing particles, classifying them based on their kinematic and geometric properties. Additionally, 'Electron-Photon Separation' algorithms help resolve ambiguous event topologies, such as distinguishing single-electron tracks from photon-induced showers. By leveraging a vast set of specialised algorithms, including 'Hierarchy Building', 'Final Particle Identification' and 'Energy Assignment techniques' and employing a modular framework, Pandora provides MicroBooNE with a highly efficient and adaptable event reconstruction tool[53].

3 CC3π^+ Selection

The signal definition for the project is the following:

$$\nu_\mu + N \rightarrow \mu + 3\pi^+ + X \tag{13}$$

where ν_μ is the muon neutrino, N shows the nucleus of the argon atoms, μ is the single muon, $3\pi^+$ are the charged pions and X indicates any particles that are not charged pions or muons. Charged pions can be either + or - as MicroBooNE is unable to determine the charge of the particle.

In this analysis, the signal definition targets charged-current interactions of muon neutrinos (ν_μ) with argon nuclei that produce a single muon and exactly three charged pions (π^+ or π^-) in the final state. This topology, often referred to as $CC3\pi^+$ represents a subset of multi-pion charged-current interactions and is characteristic of more intricate neutrino-nucleus dynamics, including resonant and deep inelastic scattering processes followed by hadronic reinteractions within the nuclear medium. The signal is inclusive with respect to other final-state particles; such as protons or electromagnetic activity as long as there is precisely one muon and three charged pions and no additional muons or charged leptons are present. To ensure a high-quality selection of events with this complex final state, several selection criteria are imposed. Events are selected by requiring a reconstructed interaction vertex inside the fiducial volume of the detector and a clearly identified muon. A topological cut is used to pick out events with multiple particle tracks, consistent with complex hadronic activity. The event must contain exactly three tracks identified as charged pions. Lastly, a cut to allow at most one of the tracks outside the fiducial volume of the detector is applied.

Therefore the full set of cuts are the following:

- 3 Charged Pions
- Maximum Uncontainment = 1
- Reconstructed vertex in Fiducial Volume
- Muon Candidate in Selection
- A Topological Cut

Firstly, a critical criterion is the identification of exactly three charged pions in the final state. To achieve this, a detailed analysis is performed on the tracks in the event, using several conditions to ensure the tracks meet the expected characteristics of pions. First, each track is evaluated based on its distance from the reconstructed neutrino interaction vertex, with a maximum allowed separation of 9.5 cm. This ensures that the tracks are consistent with originating from the same interaction. A track is then considered a potential pion candidate if it satisfies a series of conditions, including a likelihood ratio Particle Identification(PID) score greater than 0.1, classification as a second-generation particle, a track score above 0.5 setting reasonable proximity to the neutrino vertex. The cut thresholds were chosen to ensure consistency with previous pion selection studies[9][54]. The track is further required to be directly originating from the neutrino interaction, as indicated by the alignment of its start position with the simulated neutrino vertex. Additionally, to validate the true identity of the pion, a check is performed on whether the track is backtracked to the correct pion Particle Data Group (PDG) code ± 211, confirming the particle's identity as a pion. Only tracks that pass all these conditions,while ensuring containment, are counted as pions. Any track identified as the muon is excluded from the pion count. The final step in the process ensures that exactly three pion tracks are identified, forming the backbone of the event selection for multi-pion charged-current interactions. This cut allows for the precise identification of the pion components in the final state, critical for isolating the desired signal topology in the analysis.

Secondly, the selection includes a cut to ensure that no more than one primary track is uncontained, meaning the track does not fully lie within the detector's fiducial volume. For each reconstructed track, the endpoint is evaluated to check if it extends beyond the detector's boundaries. However, these uncontained tracks are only considered for inclusion in the analysis if they meet certain criteria: the track must be a valid reconstructed particle and it should have a measurable length. It must be classified as a second-generation particle, which indicates that it originates from a neutrino interaction and it must have a track score above 0.5, ensuring that the track is well-reconstructed. The selection allows for a maximum of one uncontained track in each event, accommodating minor inefficiencies in tracking and containment and still ensuring that most of the final-state particles are well-reconstructed as well as fully contained within the detector. This criterion helps preserve the integrity of the event and ensures that the analysis relies primarily on well-contained and reliable reconstructed tracks, which helps reduce background contamination and improves the precision of the signal identification.

3.1 CC Inclusive Selection

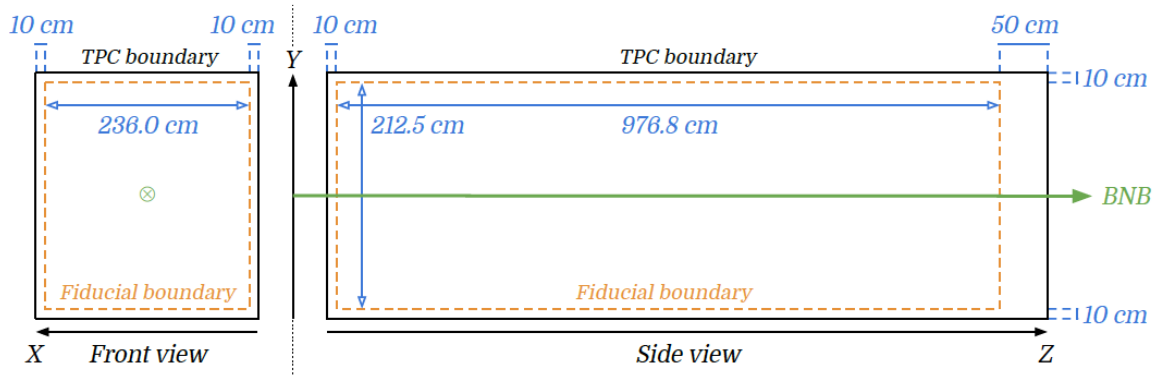

Figure 13: "The Fiducial Volume definition, shown by the dashed orange line. The black rectangle represents the full TPC volume and the green line shows the direction of the BNB." [9]

A foundational requirement of the event selection is that the reconstructed neutrino interaction vertex lies within the detector's fiducial volume. This ensures that the interaction occurs inside the instrumented region of the detector, where reconstruction is

most reliable and backgrounds from edge effects are minimised. To implement this, the three-dimensional position of the reconstructed vertex is determined using space charge-corrected coordinates and is evaluated using a geometric containment function. In liquid argon time projection chambers (LArTPCs) such as MicroBooNE, the buildup of slow-moving positive argon ions distorts the electric drift field, a phenomenon known as the space charge effect. This distortion alters the paths of ionization electrons, causing reconstructed tracks and interaction vertices to be displaced from their true positions. To address this, a space charge correction is applied using a data-driven calibration map, which restores the measured coordinates to their actual spatial values and improves the accuracy of vertex reconstruction.[42] Only events where the vertex falls entirely within this predefined fiducial region are retained for further analysis. This cut plays a critical role in ensuring data quality by rejecting events near detector boundaries, where particle tracks may be partially lost or distorted, thereby improving both the purity and reconstruction accuracy of the selected sample.

A vital element of the signal definition is the identification of a high-quality muon candidate in the final state, consistent with a charged-current muon neutrino interaction. To determine this, each reconstructed track in the event is evaluated against a set of muon identification criteria. A track is considered a muon candidate if it originates within 9.5 cm of the reconstructed neutrino vertex, ensuring spatial consistency with the interaction point. The track must also have a length greater than 20 cm and a reconstruction track quality score exceeding 0.5, which helps distinguish genuine tracks from poorly reconstructed tracks. Additionally, the track must have a log-likelihood ratio particle identification (LLR PID) score greater than 0.2 , indicating that it is more likely a muon than a proton or pion. The track must also be classified as a second-generation particle, indicating that it likely originated from the primary neutrino interaction rather than from a decay or background source. Tracks with nonphysical lengths (either zero or unrealistically large, above $1 \times 10^6 cm$) are excluded. Among all tracks that satisfy these conditions, the longest one is selected as the leading muon candidate. The presence of at least one such identified track sets the 'Muon Candidate in Selection' cut and this cut is fundamental in isolating charged-current topologies and underpins the identification of signal-like events with a muon in the final state.

In this analysis, the topological score plays a crucial role in identifying Pandora slices that are more likely to correspond to neutrino interactions. The topological score is generated by analysing various features of the slice, including particle multiplicity, directions and proximity to the detector's faces (this information is used to help distinguish between interactions occurring near the detector's edges and those occurring in the interior of the detector). These features are then fed into a Support Vector Machine (SVM), which produces a score ranging from 0 (cosmic ray-like) to 1 (neutrino-like). To ensure that only slices with a high likelihood of representing neutrino interactions are considered, a topological cut is applied to the analysis. The cut value of 0.67 is chosen for this particular analysis, meaning that only slices with a topological score greater than 0.67 are selected. This threshold helps separate neutrino-like slices from those that resemble cosmic ray events. Slices that surpass this threshold are considered to exhibit a topology consistent with neutrino interactions, particularly those involving high-multiplicity final states. As a result, the analysis only includes events where the topological score exceeds 0.67, ensuring that the majority of selected slices are likely to be true neutrino interactions, while rejecting those with a cosmic ray-like topology. This cut enhances the purity of the analysis by effectively discriminating against low-multiplicity neutrino interactions and cosmic ray contamination, thus improving the accuracy[9].

3.2 Event Displays

In this section, we look at an event display from a simulated NuMI Run 1 dataset that matches the defined signal of a muon, three charged pions and any additional particles that are neither muons nor pions. The figures below show a simulated event that illustrates this signal definition as viewed from different wire planes. The longest track is identified as the muon, consistent with its long penetrating trajectory in liquid argon. The next three longest tracks are attributed to charged pions. Other shorter tracks are likely to be protons produced from nuclear breakup. In addition to the coloured tracks, the black lines in the displays represent Monte Carlo (MC) tracks, providing a visual reference for the simulated particle trajectories. The shaded cone visible in the displays, especially in Figure 14, corresponds to a reconstructed shower, typically indicative of an electromagnetic component, such as produced by a photon

or electron. Each event is shown in the three wire planes of the MicroBooNE detector; U, V and Y planes, which provide complementary views of the same interaction and are crucial for reconstructing the full 3D geometry of the event. These displays offer a visual sense of the complex event topology and help illustrate the types of interactions selected by the analysis.

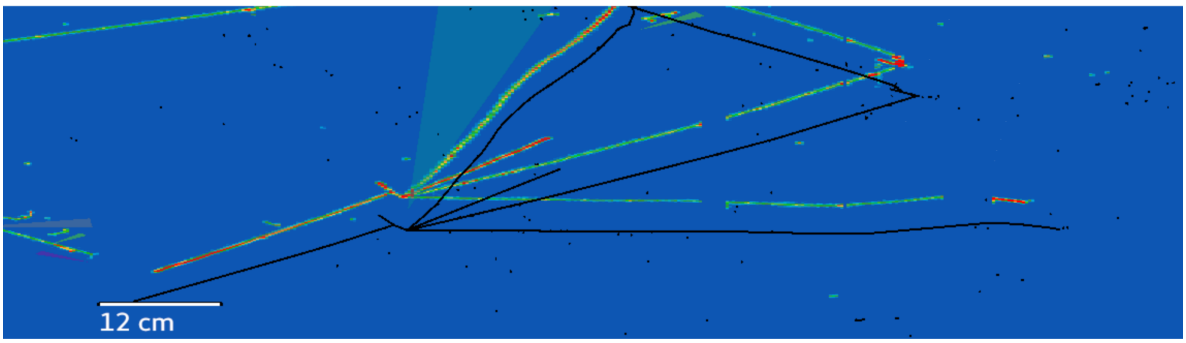

Figure 14: NuMI Run 1 EVENT:673, RUN:5189 and SUBRUN:13 - U PLANE

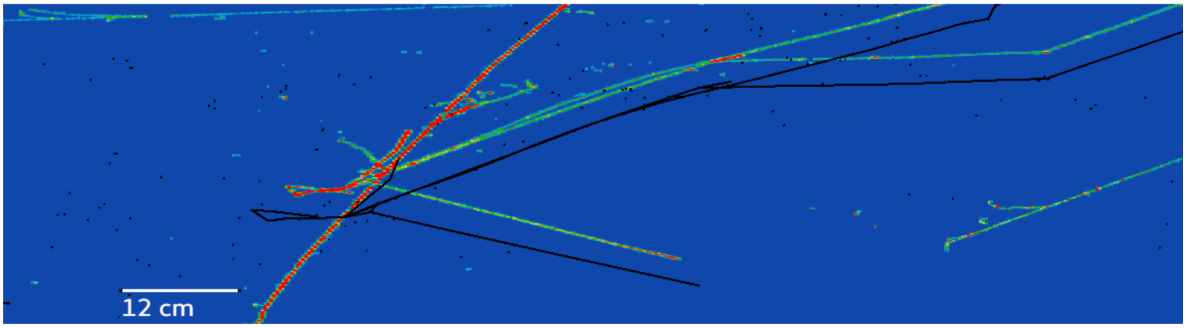

Figure 15: NuMI Run 1 EVENT:673, RUN:5189 and SUBRUN:13 - V PLANE

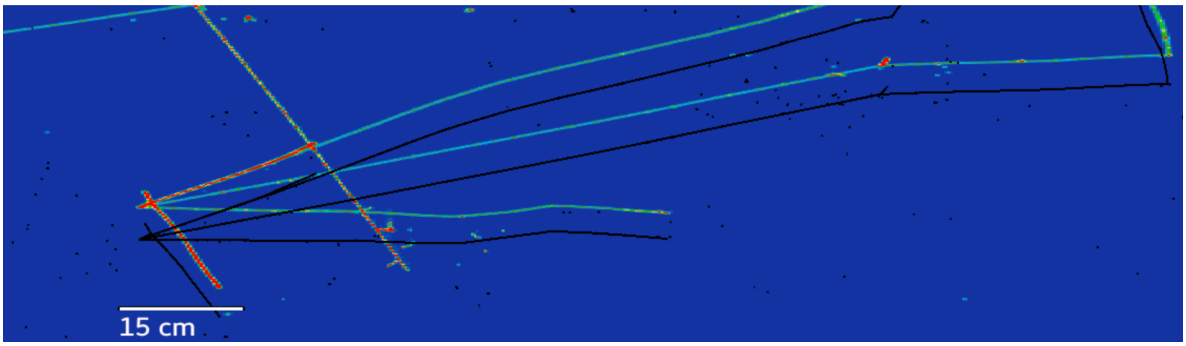

Figure 16: NuMI Run 1 EVENT:673, RUN:5189 and SUBRUN:13 - Y PLANE

3.3 Efficiency and Purity

Efficiency and purity are two cornerstone concepts in neutrino interaction analysis, especially in the context of event selection and signal identification. They serve as quantitative indicators of how well a given selection criteria performs in isolating the desired signal from the total data sample, which typically includes a mixture of signals and types of backgrounds. Both concepts play a critical role in shaping the accuracy and reliability, particularly in studies involving rare processes buried within high-background environments. Understanding efficiency and purity not only allows one to evaluate selection procedures but also helps in the estimation of systematic uncertainties, optimisation of the cuts and ultimately the precision of results such as cross-sections, branching ratios, or other calculations derived from reconstructed events.

Efficiency reflects the sensitivity of the analysis and shows how much useful data is retained. A low efficiency indicates that many potential signal events are being missed, perhaps due to overly strict cuts, limited detector coverage, or reconstruction failures. Conversely, a high efficiency implies that most signal events are being captured, maximising statistical power but potentially at the expense of introducing more background if not accompanied by stringent background suppression. The definitions of efficiency is as follows:

$$\textbf{Efficiency} = \epsilon = \frac{\text{selected signal events}}{\text{generated signal events}} \tag{14}$$

where "selected signal events" is the number of signal events that pass the selection criteria and "generated signal events" is the total number of signal events present in the dataset or simulation before selection[9].

Purity, on the other hand, quantifies the composition of the selected sample, specifically how many of the selected events are truly from the signal category. High purity means that the selected sample closely represents the physical process of interest with minimal contamination from other processes, which is essential when inferring about the nature of the signal or comparing data to theoretical predictions. Low purity, by contrast, suggests that the signal is overwhelmed by background events, making interpretation difficult and increasing the reliance on background modelling and subtraction

methods. The definitions of purity is as follows:

$$\textbf{Purity} = \rho = \frac{\text{selected signal events}}{\text{selected events}} \tag{15}$$

where "selected signal events" is the number of signal events that pass the selection and "selected events" is the total number of selected events, including both signal and background[9].

Generally, efficiency and purity are often in tension with one another. Selection strategies aiming for very high purity involve strict cuts designed to reject backgrounds with similar features to the signal. While this reduces the number of false positives, it also risks discarding genuine signal events that do not fit perfectly within the selection criteria, thus lowering efficiency. However, relaxing cuts can increase efficiency by accepting more signal events, but this usually comes at the cost of admitting more background, thereby lowering purity. This trade-off is central to the design of any analysis and requires a nuanced understanding of both the signal and background characteristics, as well as the limitations of the detector and reconstruction algorithms.

Efficiency also plays a direct role in calculating cross-sections and event rates. The cross section, which quantifies the probability of a specific interaction occurring, is not directly measurable from detector readouts alone; it must be inferred by correcting for experimental effects. This is where the efficiency of a selection becomes critical. Efficiency serves as a normalisation factor in the denominator of the cross section formula. Specifically, for a process involving a known neutrino flux ϕ and number of target nucleons T, the cross section σ is estimated using:

$$\sigma = \frac{N - B}{\epsilon \cdot \Phi \cdot T} \tag{16}$$

where N is the number of events passing selection, B is the selected background events and ϵ is the selection efficiency[33][9]. Therefore the efficiency needs to be correctly estimated to avoid the cross section being biased. Purity complements this framework by influencing the accuracy of the background subtraction itself. Since high purity ensures that a large fraction of the selected sample is composed of true signal events, it reduces the systematic uncertainty in estimating B. Together, efficiency and purity

define the reliability of the selected sample. Importantly, both are not global quantities, they vary with kinematic variables, necessitating differential assessments when performing double-differential cross-section measurements. Accurately measuring both efficiency and purity is essential in cross section analysis to make sure the results truly reflect real interaction rates, without being distorted by reconstruction errors, wrong particle IDs or selection inefficiencies[33].

In this section, we present the outcomes of the signal analysis, beginning with results from the NuMI beam followed by those from the BNB. The focus is twofold: we first examine how each individual selection cut performs in isolating the signal and then assess how these cuts function collectively when applied in sequence. This approach allows for a comprehensive evaluation of the effectiveness and impact of each criterion, as well as the overall selection strategy across both beam configurations.

3.4 Selection Results

In this section, we present the outcomes of the signal analysis, beginning with results from the NuMI beam followed by those from the BNB. The focus is twofold: we first examine how each individual selection cut performs in isolating the signal and then assess how these cuts function collectively when applied in sequence. This approach allows for a comprehensive evaluation of the effectiveness and impact of each criterion, as well as the overall selection strategy across both beam configurations. The total number of events for NuMI Run 1 is 60575.10, while BNB Run 1 contains 89555.80 events, indicating that BNB provides a larger dataset. All results presented here are based on scaled data to allow for consistent comparison between runs. Specifically, the scaling accounts for differences in exposure, with weights applied using a factor of 8.58×10^{-2}, ensuring that the effective event counts are normalised to a common basis.

3.4.1 Neutrinos at the Main Injector (NuMI)

Table 1 presents the performance of individual selection cuts for the NuMI Run 1 analysis. It shows the total number of events, signal events, events passing and failing specific cuts, as well as efficiency, purity and their product. The selection cuts include Fiducial Volume, Muon Candidate in Selection, Topological Cut, 3 pions cut and Uncontained <= 1. For each cut, the table reports the total events, the number of signal

and background events passing the cuts and the corresponding efficiency and purity values. The efficiency values range from 12.48% for the "3 pions cut" to 89.30% for the "uncontained <= 1" cut, while the purity values are generally low, indicating the challenge of reducing background contamination.

NuMI Run 1							
Selection Cuts	Total Events	Total Signal Events	Signal Events Passing Cut	Background Events Failing Cut	Efficiency	Purity	Efficiency*Purity
Fiducial Volume (Reconstructed)	60575.10	62.58	53.30	10551.10	85.19%	0.50%	0.43%
Muon Candidate in Selection	60575.10	62.58	47.04	18162.90	75.17%	0.26%	0.19%
Topological Cut	60575.10	62.58	44.12	9428.41	70.51%	0.46%	0.33%
3 Pions Cut (Contained)	60575.10	62.58	7.81	170.47	12.48%	3.35%	0.42%
Uncontained ≤ 1	60575.10	62.58	55.88	58706.00	89.30%	0.10%	0.08%

Table 1: Performance of individual cuts for NuMI Run 1

Table 2 presents the sequential performance of selection cuts applied to data from NuMI Run 1, evaluating their impact on signal retention and background suppression. The initial "fiducial volume" cut retains 85.19% of the signal events, but with a low purity of 0.50%, highlighting the presence of significant background. The "muon candidate" selection cut slightly reduces efficiency to 72.57% while marginally improving purity to 0.59%. The topological cut leads to a notable reduction in efficiency to 61.45% but enhances purity to 0.9%, indicating more effective background rejection. The 3 pions containment cut marks a drastic tightening of selection criteria, resulting in only 9.6% signal efficiency but raising purity to 5.63%, the highest in the sequence. Finally, the maximum 1 or less uncontained track requirement yields a small but cleaner sample with 8.09% efficiency and 5.17% purity. Overall, the progression of cuts reflects a typical trade-off between efficiency and purity, with tighter cuts increasingly filtering out background at the expense of losing signal. This is shown by the growing values of the efficiency*purity product.

NuMI Run 1							
Selection Cuts	Total Events	Total Signal Events	Signal Events Passing Cut	Background Events Failing Cut	Efficiency	Purity	Efficiency*Purity
Fiducial Volume (Reconstructed)	60575.10	62.58	53.30	10551.10	85.19%	0.50%	0.43%
Muon Candidate in Selection	60575.10	62.58	45.41	7668.15	72.57%	0.59%	0.43%
Topological Cut	60575.10	62.58	38.45	4244.46	61.45%	0.89%	0.55%
3 Pions Cut (Contained)	60575.10	62.58	6.01	44.21	9.60%	5.63%	0.54%
Uncontained ≤ 1	60575.10	62.58	5.06	35.36	8.09%	5.17%	0.42%

Table 2: Performance of cuts in sequence for NuMI Run 1

3.4.2 Beam Neutrino Beam (BNB)

In Table 3 the individual cuts in the BNB Run 1 analysis impact selection performance differently. The "fiducial volume" cut maintains strong efficiency but has low purity due to significant background inclusion. The "muon candidate" cut slightly reduces efficiency with minimal purity improvement. The topological cut strikes a balance, offering moderate efficiency with some purity gain. The 3 pions contained cut greatly enhances purity but reduces efficiency. Finally, the "uncontained (<= 1)" cut provides the highest efficiency but suffers from very low purity, showing a trade-off between broad inclusiveness and selectivity.

BNB Run 1							
Selection Cuts	Total Events	Total Signal Events	Signal Events Passing Cut	Background Events Failing Cut	Efficiency	Purity	Efficiency*Purity
Fiducial Volume (Reconstructed)	89555.80	43.78	36.14	16494.40	82.55%	0.22%	0.18%
Muon Candidate in Selection	89555.80	43.78	32.02	28670.00	73.14%	0.11%	0.08%
Topological Cut	89555.80	43.78	29.10	14407.30	66.47%	0.20%	0.13%
3 Pions Cut (Contained)	89555.80	43.78	6.27	168.93	14.31%	2.95%	0.42%
Uncontained ≤ 1	89555.80	43.78	40.34	87150.00	92.16%	0.05%	0.04%

Table 3: Performance of individual cuts for BNB Run 1

Table 4 presents the performance of sequential selection cuts for BNB Run 1, showing how each cut impacts the signal and background events. The "fiducial volume" cut retains a high number of total events but yields low purity, as it includes significant background. The "muon candidate" cut reduces both the total number of passing events and efficiency, with only a slight improvement in purity. The topological cut further reduces efficiency but slightly increases purity, indicating better separation of signal from background. The "3 pions cut" significantly lowers the number of passing events but enhances purity, as it suppresses background effectively. Finally, the "uncontained (<= 1)" cut offers a similar trend, with a small efficiency loss and a modest increase in purity. Overall, the sequence of cuts reflects the trade-offs between event inclusion and background rejection, with the most significant changes in efficiency and purity occurring with the more stringent cuts like "3 pions cut" and uncontained tracks.

In the comparison of the performance of cuts in sequence between NuMI Run 1 and BNB Run 1, both datasets show similar trends in cut performance. For the "fiducial volume" cut, NuMI has higher efficiency at 85.19% compared to BNB's 82.55%, but both have low purity (0.5% for NuMI, 0.22% for BNB). The "muon candidate" cut shows better efficiency for NuMI at 72.57% versus BNB's 70.98%. The topological cut has slightly better performance for NuMI compared to BNB. The "3 pions cut" shows higher efficiency and purity for BNB (11.76% efficiency, 6.26% purity) compared to

NuMI. In conclusion, while both datasets exhibit similar trends, BNB Run 1 has higher efficiency for certain cuts, while NuMI Run 1 shows better signal-background separation in others.

BNB Run 1							
Selection Cuts	Total Events	Total Signal Events	Signal Events Passing Cut	Background Events Failing Cut	Efficiency	Purity	Efficiency*Purity
Fiducial Volume (Reconstructed)	89555.80	43.78	36.14	16494.40	82.55%	0.22%	0.18%
Muon Candidate in Selection	89555.80	43.78	31.07	12376.00	70.98%	0.25%	0.18%
Topological Cut	89555.80	43.78	25.92	6764.81	59.21%	0.38%	0.23%
3 Pions Cut (Contained)	89555.80	43.78	5.15	38.54	11.76%	6.26%	0.74%
Uncontained ≤ 1	89555.80	43.78	4.29	33.39	9.80%	5.56%	0.54%

Table 4: Performance of cuts in sequence for BNB Run 1

3.5 Boosted Decision Tree (BDT)

A Boosted Decision Tree (BDT) is an advanced machine learning technique widely used for classifying events, particularly in distinguishing signal from background[55]. The foundation of this method lies in the decision tree; a straightforward classifier that repeatedly partitions a labelled dataset of signal and background events using input variables chosen for their ability to separate the two classes. At each branching point, the algorithm identifies the most effective variable and threshold to split the data, aiming to increase the purity of signal or background in each resulting subset. This splitting continues until the data within each terminal node, is mostly uniform. However, individual decision trees are often vulnerable to statistical noise and variations within the training sample. To address this, the BDT approach constructs an ensemble of trees, where each new tree is trained on a modified dataset that emphasises previously misclassified events. By combining the output of all trees weighted according to their accuracy, the BDT forms a more resilient and accurate classifier. This significantly enhances overall performance and reduces sensitivity to fluctuations in the training data.

In Figure 17, the BDT response illustrates a clear separation between signal and background events, with the signal peaking at higher response values. Figure 18 verifies training reliability via an overtraining check, showing strong agreement between training and testing samples, particularly for the signal. Figure 19 and Figure 20 offer Receiver Operating Characteristic (ROC) metrics to assess performance. Figure 19 maps background rejection against signal efficiency, showing a steep curve that reflects the model's ability to suppress background without heavily sacrificing the signal. Lastly, Figure 20 which exhibits 1/(background efficiency) versus signal efficiency, highlights classifier strength in rejecting background even at low signal efficiencies, critical in analyses where background must be tightly controlled.

Muons and pions are generally classified as Minimum Ionising Particles (MIPs) in many detector systems, including MicroBooNE. When developing identification cuts and training MIP-focused BDTs, these particles are treated as MIPs due to their relatively low and consistent energy deposition, which helps distinguish them from more heavily ionising particles such as protons or electrons. Hence the minimum ionising particles (MIPs) BDT was incorporated into my analysis code when determining the muon and pion identification selection criteria. Therefore, (MIPs) BDT was applied specifically to the 'muon candidate' in selection cut and the '3 charged pions' selection cut. The BDT output variable (tmvaoutput) was used as a key discriminator in the selection process. A cut value of 0.1 was chosen based on the distributions shown in Figure 17 and Figure 18, where a clear signal peak is observed around 0.1. This specific value was selected to align with the characteristic behaviour of the signal, making it a natural choice for defining the cut.

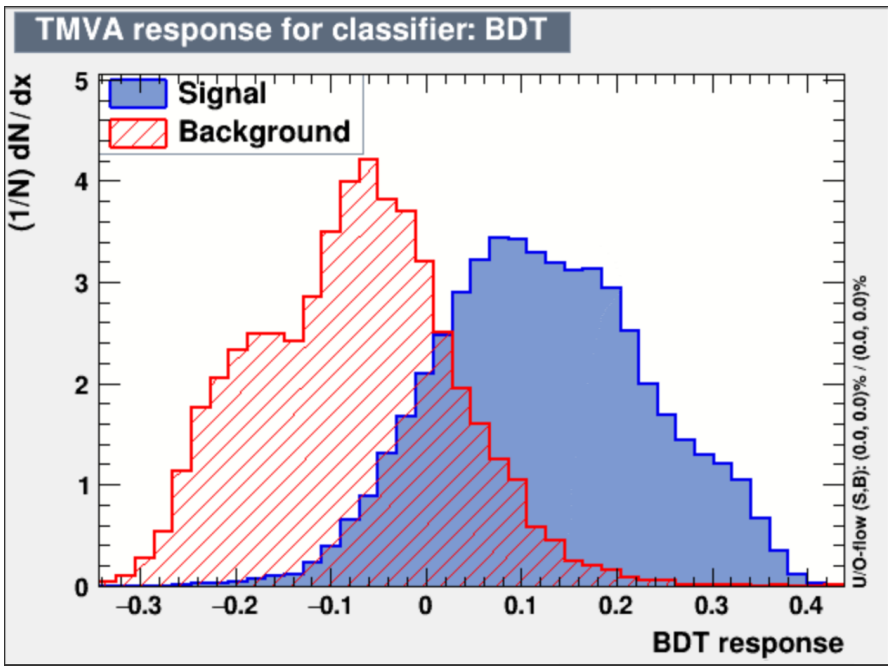

Figure 17: BDT Response Distribution.

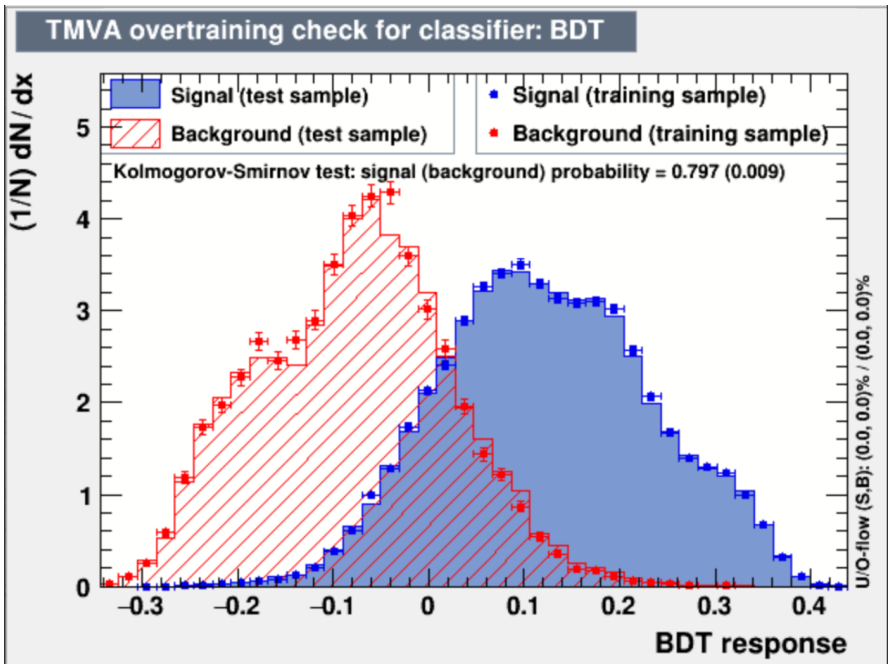

Figure 18: Overtraining Check: Comparison of BDT response for training and test datasets.

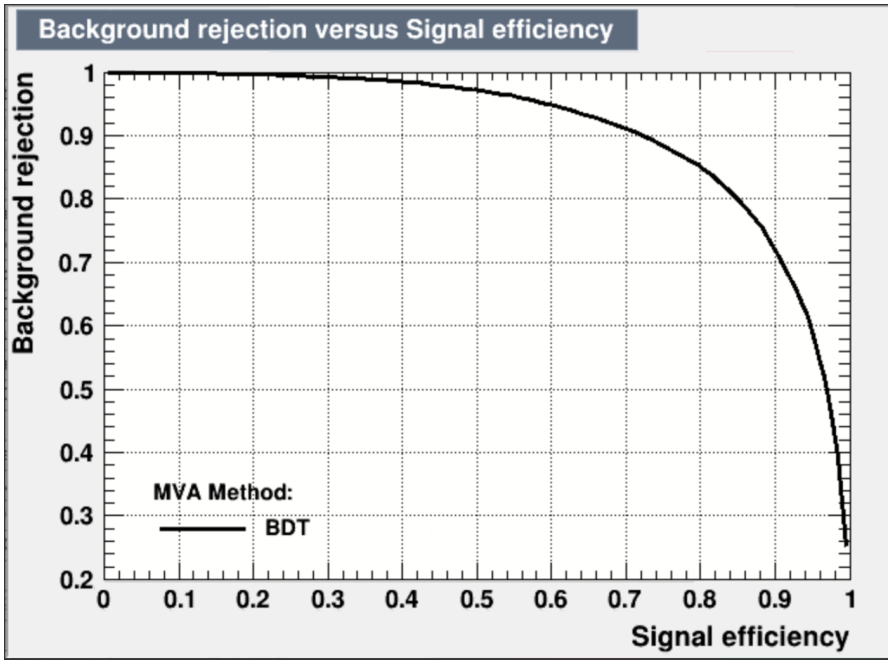

Figure 19: (ROC) curve showing background rejection versus signal efficiency.

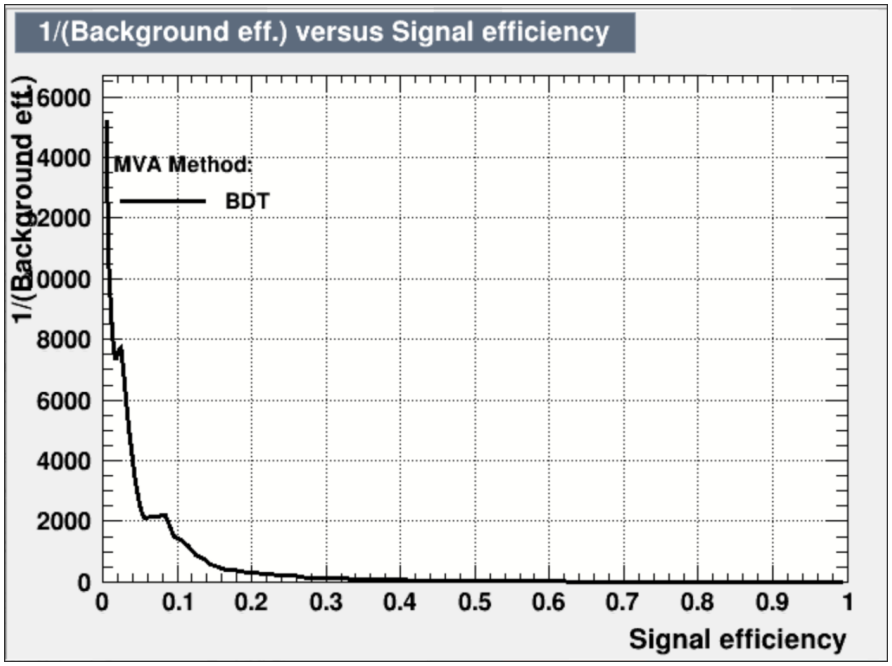

Figure 20: Inverse Background Efficiency vs. Signal Efficiency.

Table 5 shows how the introduction of a BDT affects event selection compared to the baseline (no BDT) NuMI Run 1 data. Across most cuts, the efficiency values remain consistent, particularly for the fiducial volume and topological cuts, which see identical performance between the two datasets. However, the clearest BDT-driven improvement

appears in the "3 pions cut", where although the signal efficiency drops from 12.48% to 7.13%, the signal purity improves from 3.35% to 3.17%. This small increase in purity suggests that the BDT is better at rejecting background in this region, albeit at the cost of retaining fewer signal events. Interestingly, the product of efficiency and purity decreases slightly from 0.42% to 0.23%, indicating a modest trade-off. Earlier cuts, such as the "muon candidate" selection, show minimal changes, with a small dip in efficiency (from 75.17% to 73.94%) and essentially unchanged purity. These results imply that the BDT has the most significant impact when sculpting the final signal region.

NuMI Run 1 BDT							
Selection Cuts	Total Events	Total Signal Events	Signal Events Passing Cut	Background Events Failing Cut	Efficiency	Purity	Efficiency*Purity
Fiducial Volume (Reconstructed)	60575.10	62.58	53.30	10551.10	85.19%	0.50%	0.43%
Muon Candidate in Selection	60575.10	62.58	46.27	17505.00	73.94%	0.26%	0.19%
Topological Cut	60575.10	62.58	44.12	9428.41	70.51%	0.46%	0.33%
3 Pions Cut (Contained)	60575.10	62.58	4.46	78.20	7.13%	3.17%	0.23%
Uncontained ≤ 1	60575.10	62.58	55.88	58706.00	89.30%	0.10%	0.08%

Table 5: Performance of individual cuts for NuMI Run 1 BDT

The implementation of BDT in the BNB Run 1 data reveals notable differences in individual cut performance when compared to the baseline dataset without BDT as seen in Table 6, the efficiency values remain similar, particularly for early cuts like the "fiducial volume" and "muon candidate" selections. However, the BDT enhances background rejection capabilities at later stages. Most notably, the "3 pions cut" sees a significant drop in signal efficiency (from 14.31% without BDT to 7.06% with BDT), but this comes with a small drop in purity (from 2.95% to 2.55%), indicating improved background suppression. This illustrates the BDT's strength in refining the signal region, even if it reduces the overall number of retained signal events.

BNB Run 1 BDT							
Selection Cuts	Total Events	Total Signal Events	Signal Events Passing Cut	Background Events Failing Cut	Efficiency	Purity	Efficiency*Purity
Fiducial Volume (Reconstructed)	89555.80	43.78	36.14	16494.40	82.55%	0.22%	0.18%
Muon Candidate in Selection	89555.80	43.78	30.90	27655.60	70.59%	0.11%	0.08%
Topological Cut	89555.80	43.78	29.10	14407.30	66.47%	0.20%	0.13%
3 Pions Cut (Contained)	89555.80	43.78	3.09	77.25	7.06%	2.55%	0.18%
Uncontained ≤ 1	89555.80	43.78	40.34	87150.00	92.16%	0.05%	0.04%

Table 6: Performance of individual cuts for BNB Run 1 with BDT

In Table 7, the sequential cutflow for NuMI Run 1 using the BDT model shows a trade-off between signal efficiency and background rejection when compared to the baseline (non-BDT) selection. In the early stages, such as after the "fiducial volume" and "muon candidate" cuts, both approaches perform nearly identically, with efficiencies of about 85% and $\sim$ 71–73% respectively, and purities remaining under 1%. As cuts become more restrictive, however, differences emerge. After the "3 pions cut", the non-BDT selection retains 6.01 signal events with a purity of 5.63%, whereas the BDT keeps only 3.69 signal events but with a slightly lower purity of 4.36%. This reduction in purity and efficiency continues in the final stage: the "uncontained <= 1" cut leaves the BDT selection with 3.26 signal events (efficiency 5.21% and a purity of 4.10%), compared to 5.06 signal events (efficiency 8.09% and 5.17% purity) without BDT. Consequently, while the baseline selection consistently achieves higher signal efficiency and better purity in the late stages, the BDT produces a smaller, more restrictive sample. The efficiency–purity product also reflects this, remaining stronger in the non-BDT case (0.42% compared to 0.21% in the final cut), suggesting that in this configuration the BDT sacrifices too many signal events without sufficiently compensating gains in background suppression.

NuMI Run 1 BDT							
Selection Cuts	Total Events	Total Signal Events	Signal Events Passing Cut	Background Events Failing Cut	Efficiency	Purity	Efficiency*Purity
Fiducial Volume (Reconstructed)	60575.10	62.58	53.30	10551.10	85.19%	0.50%	0.43%
Muon Candidate in Selection	60575.10	62.58	44.64	7410.13	71.33%	0.60%	0.43%
Topological Cut	60575.10	62.58	37.94	4117.08	60.63%	0.91%	0.55%
3 Pions Cut (Contained)	60575.10	62.58	3.69	22.06	5.90%	4.36%	0.26%
Uncontained ≤ 1	60575.10	62.58	3.26	16.91	5.21%	4.10%	0.21%

Table 7: Performance of cuts in sequence for NuMI Run 1 with BDT

In Table 8, the sequential cutflow for BNB Run 1 using the BDT model shows a consistent reduction in signal efficiency relative to Table 4, while also yielding lower purities at the final stages of selection. Both methods perform identically at the "fiducial volume" cut, with an efficiency of 82.55% and purity of 0.22%. Differences appear at the "muon candidate" stage: the baseline selection retains 70.98% of the signal with a purity of 0.25%, compared to 68.82% efficiency and the same purity under the BDT. As cuts become more restrictive, the BDT consistently accepts fewer signal events—dropping from 25.92 to 25.06 after the "topological cut" and from 5.15 to only 2.66 after the "3 pions cut". This reduction in signal is accompanied by lower purity as well: at the "3 pions cut", purity falls from 6.26% in the baseline to 4.34% with BDT. By the final "uncontained <= 1" cut, the non-BDT selection maintains 4.29 signal events with 5.56% purity, while the BDT leaves just 2.15 signal events and 3.67% purity. The efficiency–purity product likewise decreases from 0.54% (non-BDT) to 0.18% (BDT). Overall, the BDT approach in BNB Run 1 does not yield drastic improvements in purity instead producing a more restrictive selection that reduces both efficiency and purity in the final stages.

BNB Run 1 BDT							
Selection Cuts	Total Events	Total Signal Events	Signal Events Passing Cut	Background Events Failing Cut	Efficiency	Purity	Efficiency*Purity
Fiducial Volume (Reconstructed)	89555.80	43.78	36.14	16494.40	82.55%	0.22%	0.18%
Muon Candidate in Selection	89555.80	43.78	30.13	11985.00	68.82%	0.25%	0.17%
Topological Cut	89555.80	43.78	25.06	6581.29	57.25%	0.38%	0.22%
3 Pions Cut (Contained)	89555.80	43.78	2.66	17.60	6.08%	4.34%	0.26%
Uncontained ≤ 1	89555.80	43.78	2.15	14.68	4.90%	3.67%	0.18%

Table 8: Performance of cuts in sequence for BNB Run 1 with BDT

3.6 Pion Analysis

Across all selection performance tables reviewed earlier, a consistent and significant efficiency drop was observed following the application of the "3 pion cut" in the sequential analysis. As cuts were added in sequence, starting from fiducial volume, through muon identification, topological score and finally the "3 pion cut" cut repeatedly emerged as the most critical point of efficiency loss. This prompted a focused investigation into the behavior of charged pions within the signal definition. To better understand the underlying cause of this drop, a analysis was performed on a series of pion-related distributions including track score, pion generation, distance from the neutrino interaction vertex and most importantly momentum; examined both from MC truth and backtracked momentum. This analysis was performed for both the NuMI and BNB beam modes. As shown in the histograms below, the BNB data contains relatively few pions to begin with compared to the NuMI data, which warrants further investigation in the future. This analysis provides a comprehensive view of how pion reconstruction and selection affect signal retention across different neutrino flux conditions.

The motivation behind conducting the detailed pion analysis stems from the specific selection criteria applied to identify charged pion candidates within the dataset. The condition for pion criteria encapsulates a set of stringent requirements designed to isolate high quality pion tracks originating from the neutrino interaction vertex. These

include a log-likelihood PID score greater than 0.1, indicating a reasonable probability the particle is a pion based on its energy deposition profile; a generation value of 2, signifying that the track is a primary daughter of the neutrino interaction rather than a secondary or tertiary particle; a track score above 0.5, ensuring that the reconstructed object is indeed a well-defined track and not a shower or noise; and a proximity within 9.5 cm to the neutrino vertex, helping suppress background from unrelated or cosmic tracks. These strict requirements significantly reduce background contamination but also highlight where the efficiency drops drastically, particularly after the "3 pions cut" in the selection sequence. To better understand this loss and improve signal retention, a focused investigation was carried out examining various pion-related variables.

3.6.1 Beam Neutrino Beam (BNB)

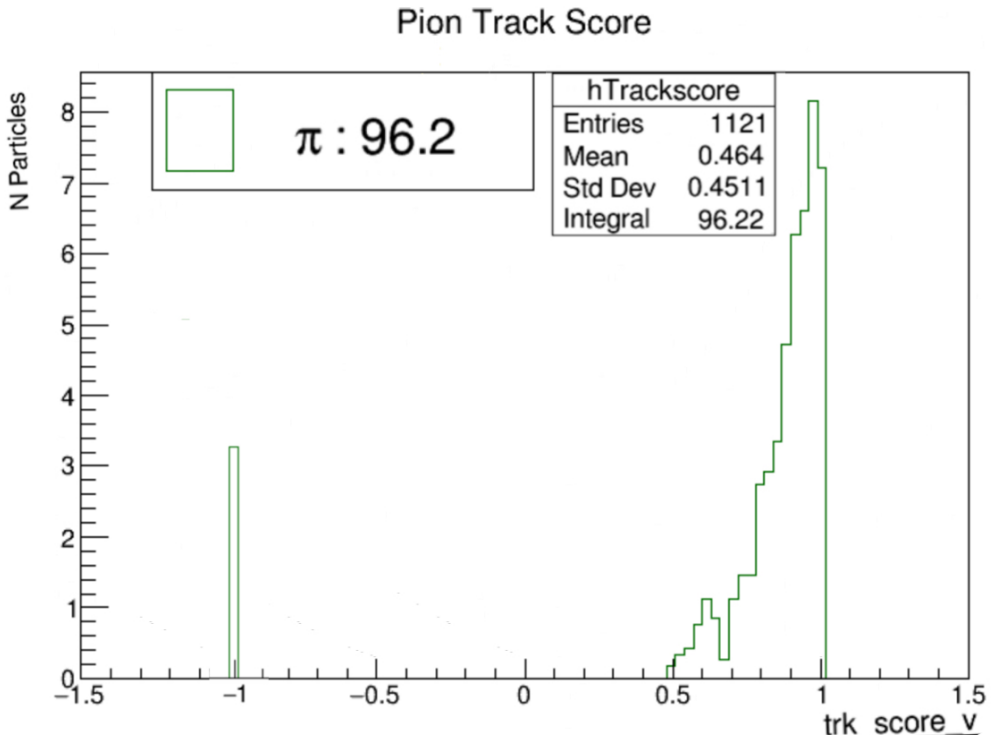

Figure 21: Histogram showing pion track score trend for BNB.

When selecting pions, a track score greater than 0.5 is required. As seen in Figure 21, the distribution peaks above this value, indicating that well-reconstructed pion tracks are predominantly found in this region. Setting the threshold at 0.5 ensures we retain

the majority of good-quality tracks while suppressing poorly reconstructed tracks.

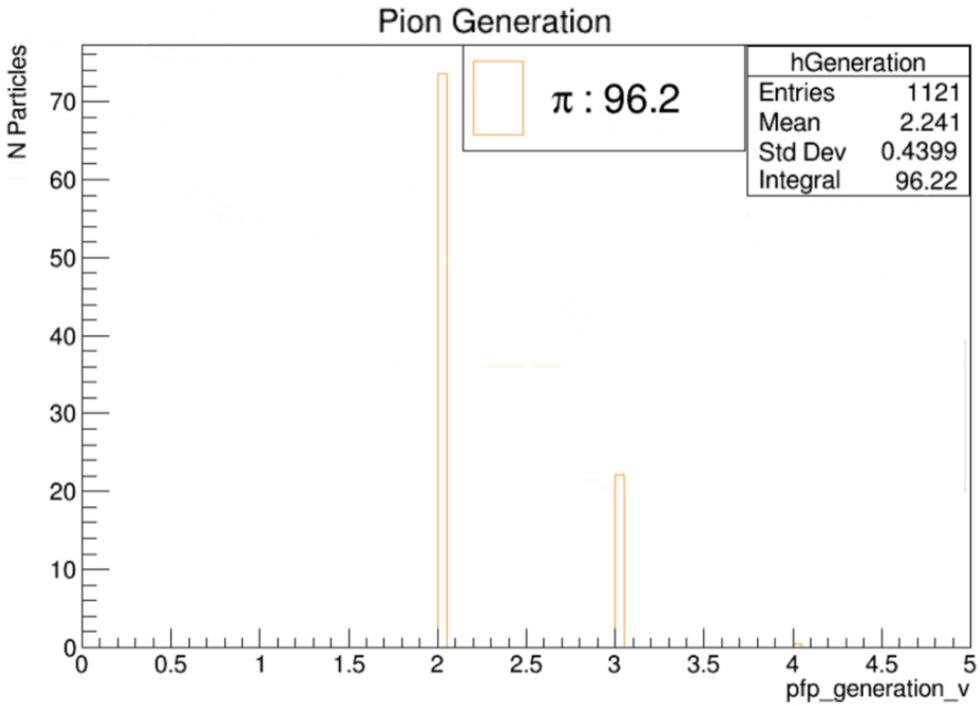

Figure 22: Histogram showing pion generation trend for BNB.

Only particles from generation 2 are retained. Figure 22 shows that the pion signal is concentrated at generation 2, suggesting that most pions of interest originate from the primary interaction or early stage decays. This selection improves the purity of the sample by excluding later generation background particles.

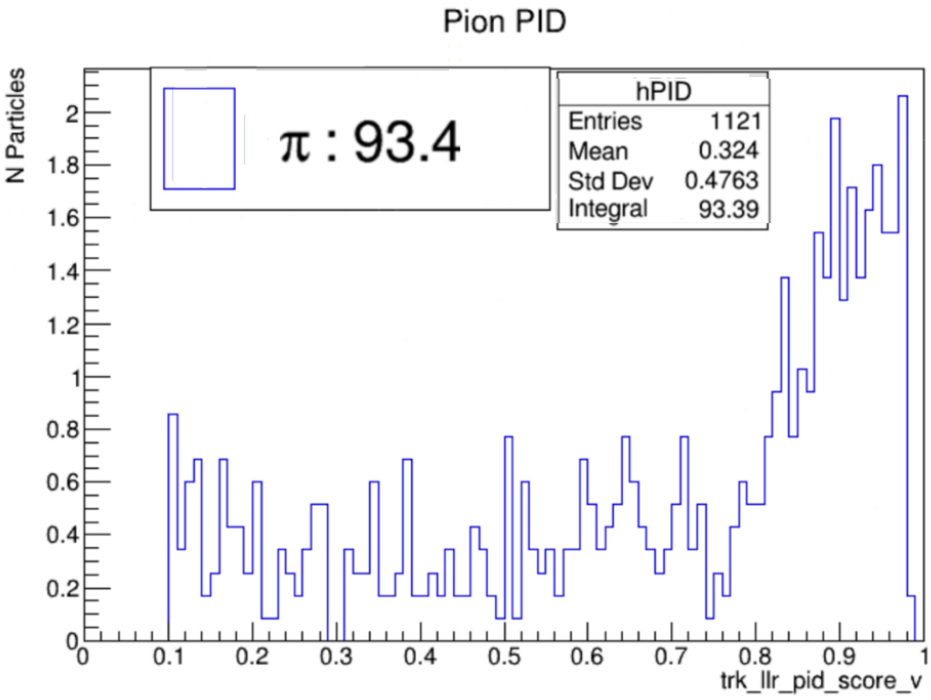

Figure 23: Histogram showing pion Log-Likelihood Ratio Particle Identification (PID) score trend for BNB.

A log-likelihood PID score greater than 0.1 is required for pion selection. As shown in Figure 23, the tracks totally lie above this value, while the background contribution is more evenly distributed or peaks at lower values. This threshold improves particle identification by favoring tracks more likely to be pions, while maintaining good signal efficiency.

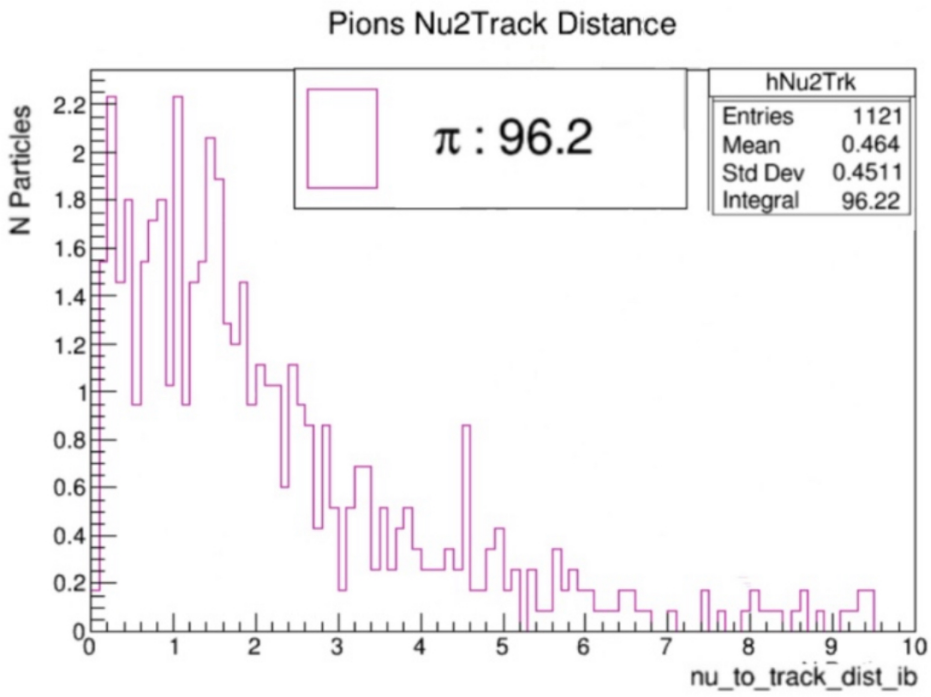

Figure 24: Histogram showing pion track distance(cm) from neutrino vertex trend for BNB.

A maximum neutrino to track distance of 9.5 cm is imposed. As shown in Figure 24, the signal contribution significantly diminishes beyond this point. This cut ensures spatial consistency between the reconstructed track and the neutrino interaction vertex, helping to suppress unassociated tracks.

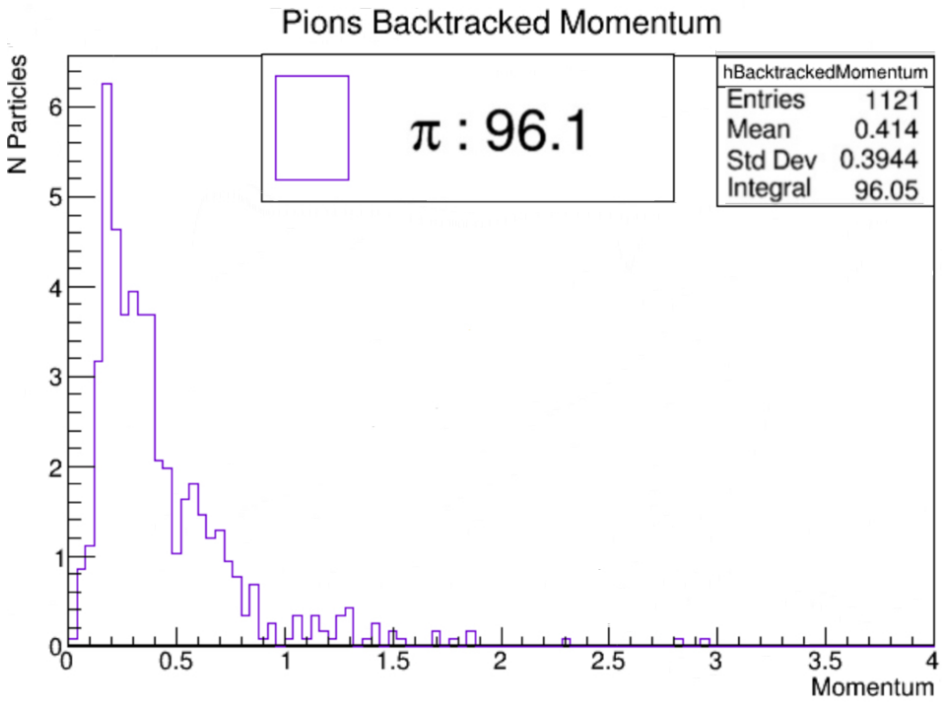

Figure 25: Histogram showing pion backtracked momentum magnitude(GeV/c) trend for BNB.

The distribution of backtracked momentum in Figure 25 shows that the majority of selected pion candidates fall below 1 GeV/c. Although not used as a strict cut, this observation confirms consistency with the expected kinematics of pions produced in neutrino interactions. Additionally, it provides insight into why some pions may be falling behind in passing as signal, which could explain the observed drop in efficiency after applying the "3 pion cut". In particular, this efficiency loss is largely driven by low momentum pions, which are more difficult to reconstruct and identify reliably.

3.6.2 Neutrinos at the Main Injector (NuMI)

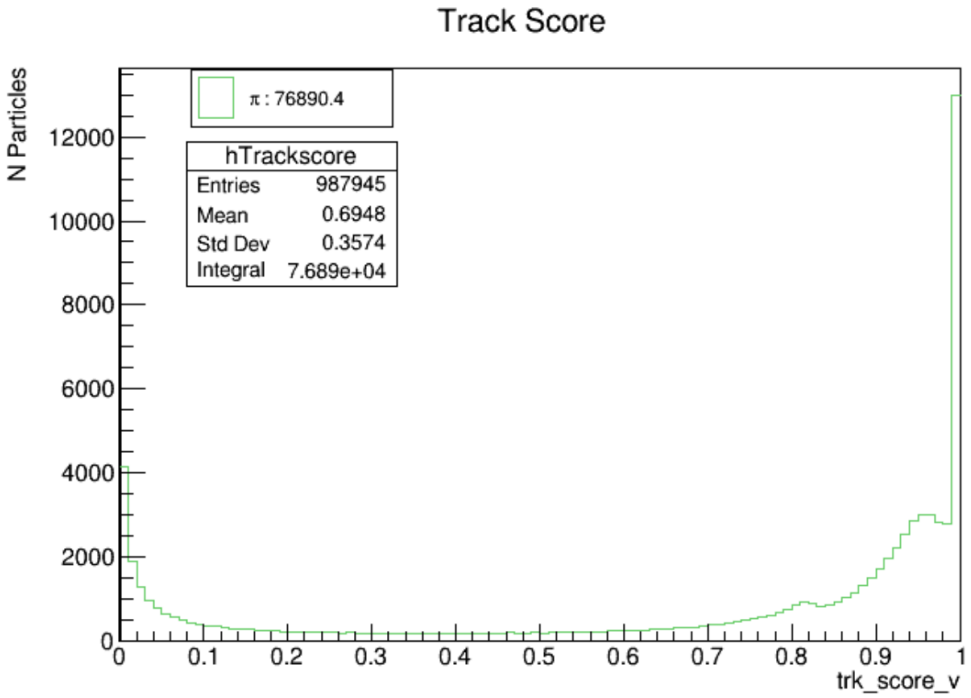

Figure 26: Histogram showing pion track score trend for NuMI.

When identifying pions, only tracks with a score more than 0.5 are considered. As shown in Figure 26, the distribution increases above this threshold, indicating that accurately reconstructed pion tracks are primarily found in this region. This behavior is similar to what is observed in BNB, where high-quality tracks also cluster above the same score. Setting the cutoff at 0.5 allows us to retain the majority of good-quality tracks while effectively suppressing poorly reconstructed ones.

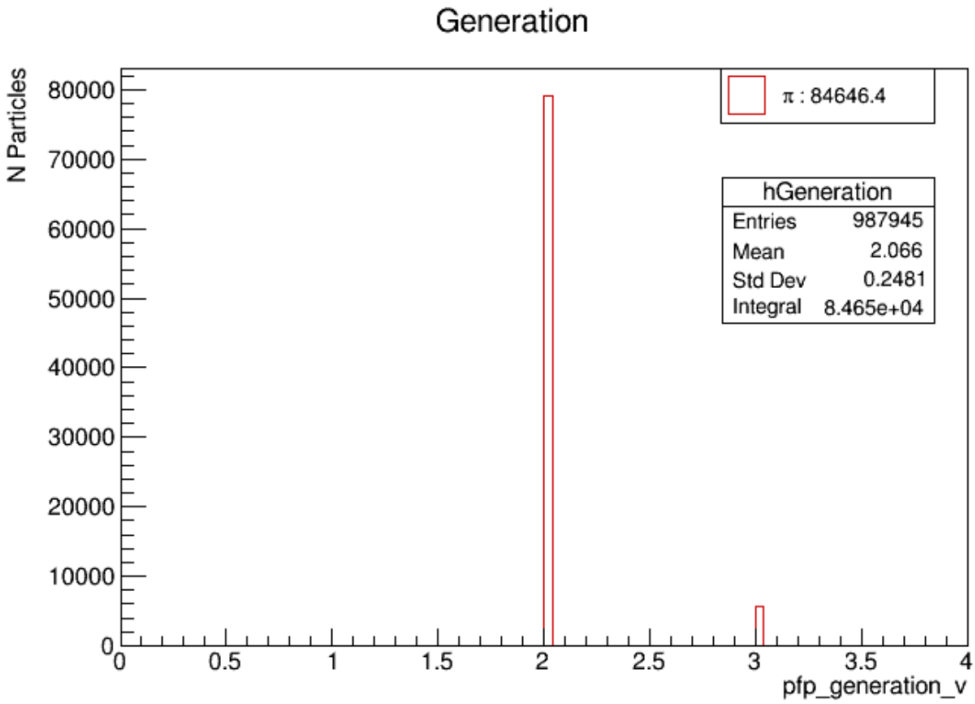

Figure 27: Histogram showing pion generation trend for NuMI.

Only particles from generation 2 are retained. Figure 27 shows that the pion signal is concentrated at generation 2, suggesting that most pions of interest originate from the primary interaction or early stage decays. This plot is almost same as the plot for BNB except few generation 3 pions are seen as well. This selection improves the purity of the sample by excluding later generation background particles.

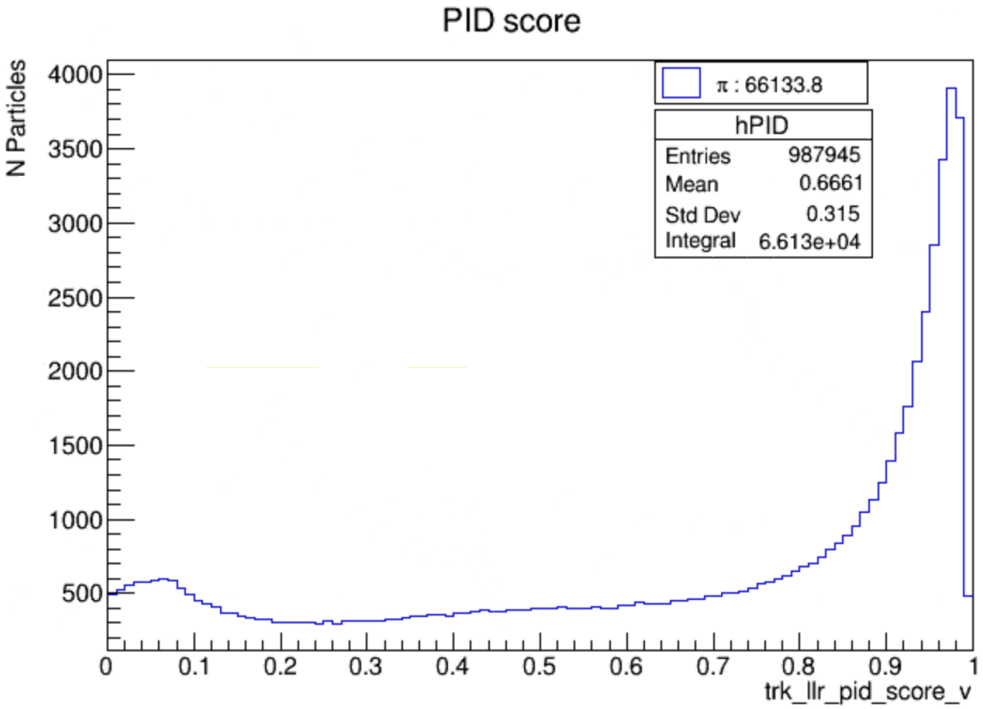

Figure 28: Histogram showing pion Log-Likelihood Ratio Particle Identification (PID) score trend for NuMI.

A log-likelihood PID score greater than 0.1 is required for pion selection. As shown in Figure 28, the tracks totally lie above this value, while the background contribution is more evenly distributed or peaks at lower values. This threshold improves particle identification by favoring tracks more likely to be pions, while maintaining good signal efficiency. In this NuMI plot a lot more pions are seen compared to BNB plot.

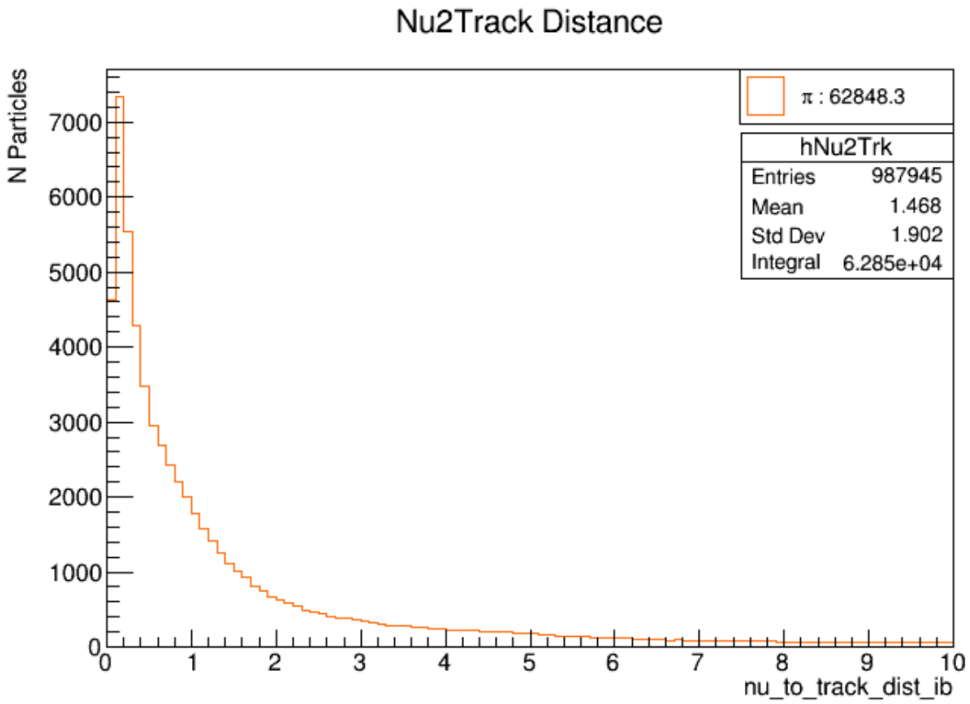

Figure 29: Histogram showing pion track distance(cm) from neutrino vertex trend for NuMI.

A maximum neutrino to track distance of 9.5 cm is imposed. As shown in Figure 29, the signal contribution significantly diminishes beyond this point. This cut ensures spatial consistency between the reconstructed track and the neutrino interaction vertex, helping to suppress unassociated tracks. Similar to Figure 24 but with more pions for this criteria.

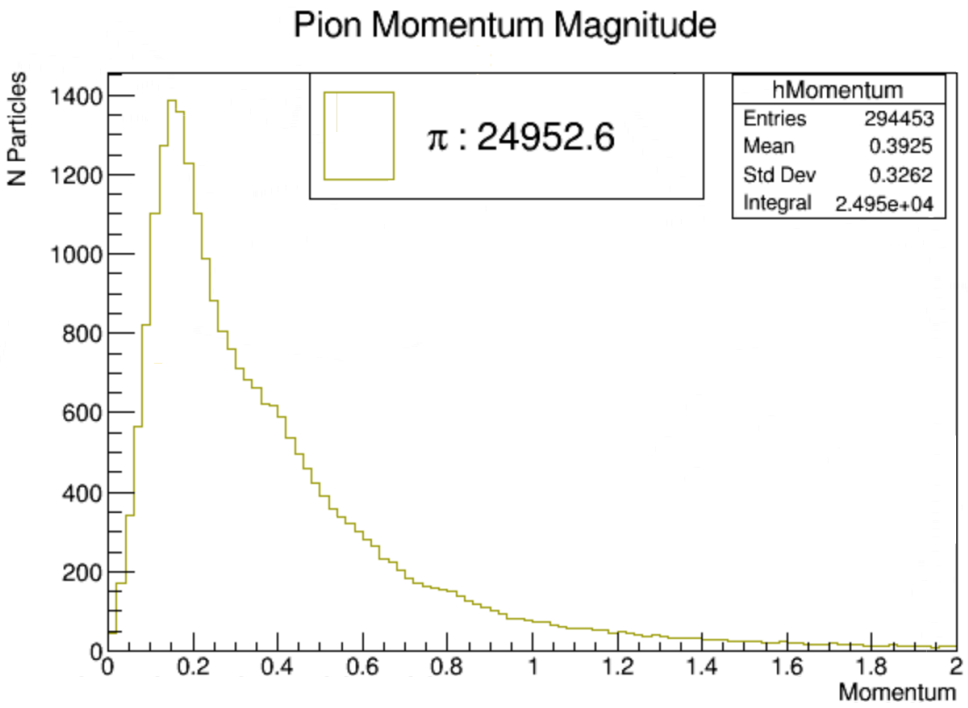

Figure 30: Histogram showing pion MC momentum magnitude(GeV/c) trend for NuMI.

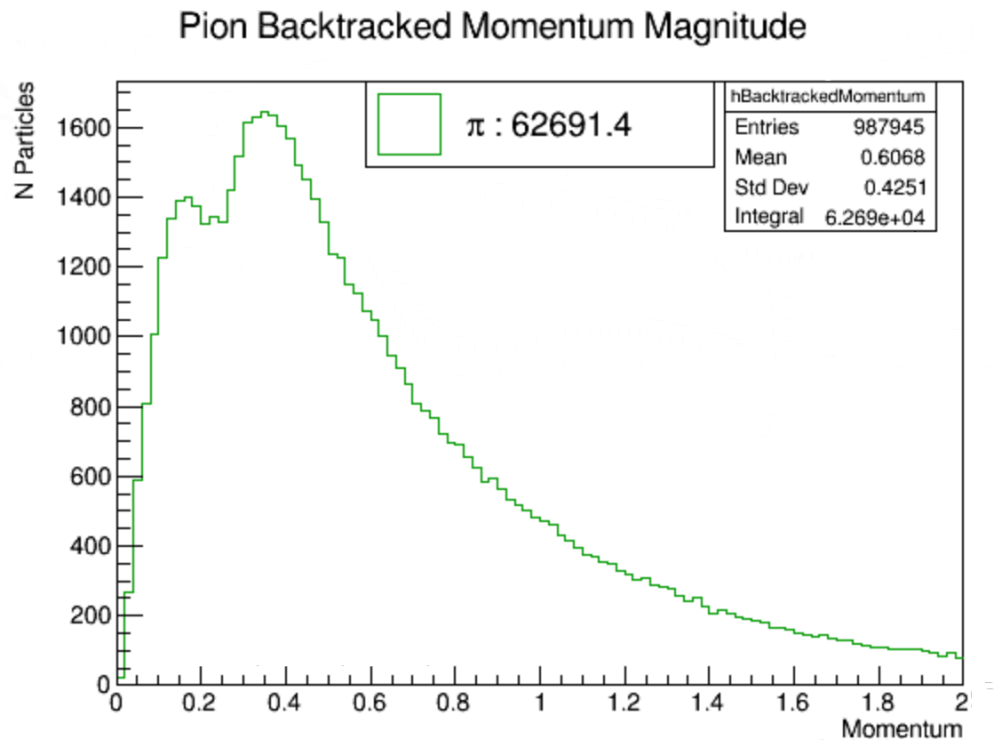

Figure 31: Histogram showing pion backtracked momentum magnitude(GeV/c) trend for NuMI.

Figures 30 and 31, which show the MC momentum magnitude and backtracked momentum magnitude respectively, exhibit a consistent trend, a gradual rise in the momentum distribution for values below 1 GeV/c. This similarity between the two distributions reinforces confidence in the reconstruction's ability to capture the underlying kinematics of pions from neutrino interactions. Although the momentum is not used as a strict selection cut, this agreement with expected pion behavior supports the validity of the selection strategy. Furthermore, it offers a possible explanation for the observed drop in efficiency after applying the "3 pion cut". Some pions may fall short of passing the full selection criteria due to their lower momenta, which could lead to them being reconstructed less efficiently or not at all.

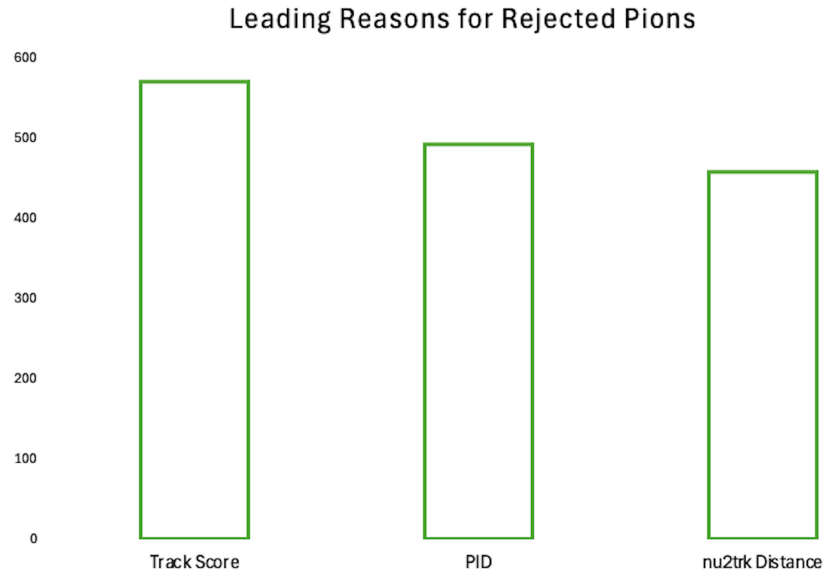

Figure 32: Leading reasons for rejected pions.

An analysis of failed pions was performed by outputting their track IDs along with track score, PID, neutrino-to-track distance, and generation. As shown in Figure 32, the primary cause of failure was most often the track score of the pions. The next main reasons for pion failure are low PID scores and failing the neutrino to track distance cut.

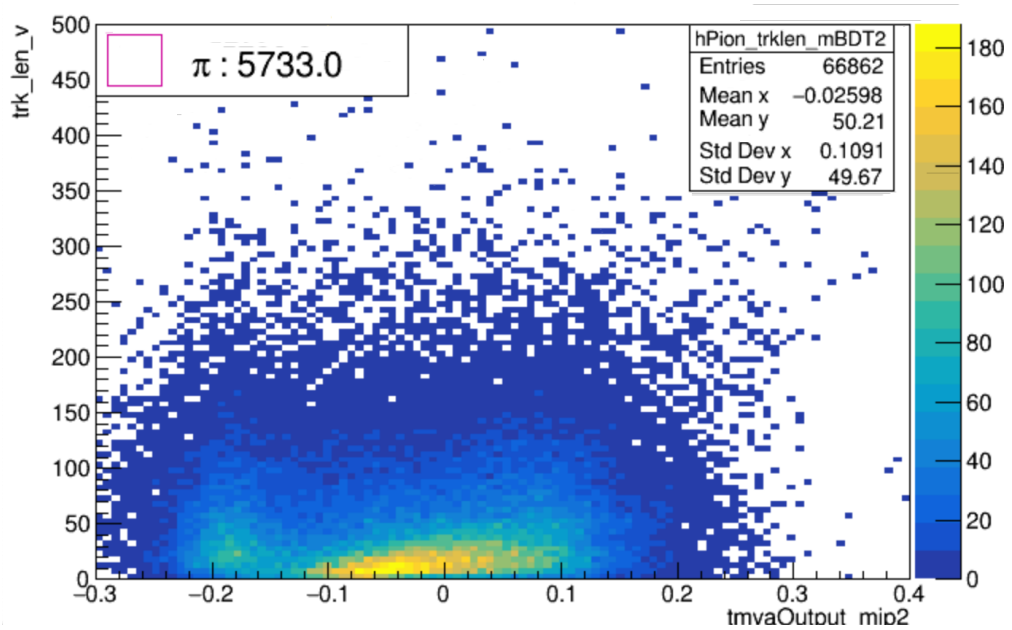

Figure 33: MIPS BDT output against BDT pions

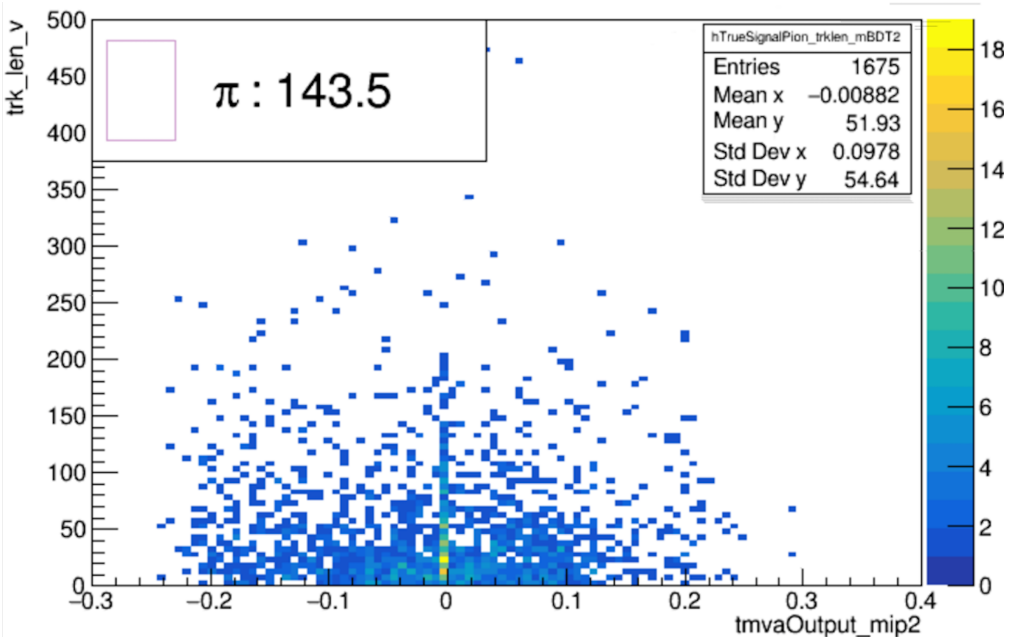

Figure 34: MIPS BDT output against true signal pions.

Figures 33 and 34 present the MIPS BDT output versus track length of pions, aimed at understanding the drop in efficiency observed after applying the "3 pions" cut in the final selection. Figure 33 shows this distribution for all BDT-selected pions, revealing a wide spread with a peak near zero and a total of 5733 entries. In contrast, Figure 34 focuses on true signal pions, those directly originating from the neutrino vertex,

with pion PDG and is signal, shows a much smaller population (143.5 pions), with the distribution tightly concentrated between -0.1 and 0.1. The sharp peak in this narrow region validates the use of -0.1 as the TMVA output threshold, as it effectively captures true signal pions. This comparison highlights that the BDT may include a substantial number of non-signal tracks and the MIPS BDT cut, though well-placed, may still exclude some true pions, helping explain the observed efficiency loss post-cut.

4 Future Research and Development

This analysis lays the groundwork for a deeper understanding of complex neutrino interactions involving multi-pion final states in liquid argon, but it also opens several promising paths for future development. For instance, incorporating an opening angle cut, an analysis technique that, while conceptually straightforward in simpler topologies, becomes increasingly intricate in the presence of three charged pions. The $CC3\pi^+$ topology introduces a non-trivial angular structure: multiple pion-pion opening angles, their individual correlations with the muon and potential secondary decay kinematics must all be considered. Developing a robust multidimensional angular selection strategy will likely require novel approaches, such as machine learning techniques that can learn from the full angular phase space or other statistical simulations. If such a cut can be successfully implemented, it could significantly enhance the signal purity by further reducing background from misidentified topologies like $CC\pi^+$ and deep inelastic scattering with neutral pion production.

Moreover, the eventual goal of this line of research is to transition from selection-level studies to differential and total cross-section measurements. With the statistical and systematic groundwork laid by this analysis, future efforts can move toward unfolding the selected data to extract cross sections for $CC3\pi^+$ interactions, a currently unmeasured but theoretically important component of the neutrino-argon interaction landscape. Such measurements will not only enrich the MicroBooNE physics program but will also serve as critical inputs for tuning interaction models in generators, particularly resonant decay dominated regions.

The complexity of the signal definition in this analysis requiring precise identification of three charged pion tracks, a muon and a consistent vertex underscores the increasing sophistication of event reconstruction in modern LArTPC experiments. It reflects a broader push within the neutrino community to explore more exclusive final states, moving beyond inclusive CC selections. These efforts are crucial for reducing model dependencies and for constraining backgrounds in oscillation measurements, especially for next-generation detectors like DUNE.

Finally, MicroBooNE continues to play a unique role as a bridge between the small-scale precision and large-scale goals of the neutrino program. The tools, techniques and lessons developed here such as multivariate analysis with boosted decision trees, and data-driven validation using both BNB and NuMI beamlines form a transferable toolkit. Future experiments will benefit directly from this foundational work, especially as they seek to characterise rare interaction modes in high-resolution detectors. In this way, the current analysis not only contributes new physics results but also helps chart a path for the increasingly complex and ambitious analyses that lie ahead in the era of precision neutrino physics.

Bibliography

[1] ATLAS Collaboration, "Standard model and beyond - ATLAS open data," 2024, accessed: 2024-03-26. [Online]. Available: https://opendata.atlas.cern/docs/documentation/introduction/SM_and_beyond

[2] K. V. J. Mistry, *Neutrino Interactions*. Cham: Springer International Publishing, 2023, pp. 15–32. [Online]. Available: https://doi.org/10.1007/978-3-031-19572-3_3

[3] Betancourt. (2019) Lepton photon 2019 pdf. Accessed: 2025-03-27. [Online]. Available: https://indico.cern.ch/event/688643/contributions/3410420/attachments/1892142/3120655/Betancourt_Lepton_Photon_2019.pdf

[4] J. A. Formaggio and G. P. Zeller, "From eV to EeV: Neutrino cross sections across energy scales," *Reviews of Modern Physics*, vol. 84, no. 3, pp. 1307–1341, 2012.

[5] MicroBooNE Collaboration, "Design and construction of the MicroBooNE detector," *Journal of Instrumentation*, vol. 12, no. 02, p. P02017–P02017, Feb. 2017. [Online]. Available: http://dx.doi.org/10.1088/1748-0221/12/02/P02017

[6] T. Briese, L. Bugel, J. Conrad, M. Fournier, C. Ignarra, B. Jones, T. Katori, R. Navarrete-Perez, P. Nienaber, T. McDonald *et al.*, "Testing of cryogenic photomultiplier tubes for the MicroBooNE experiment," *Journal of Instrumentation*, vol. 8, no. 07, p. T07005, 2013.

[7] P. Abratenko, J. Anthony, L. Arellano, J. Asaadi, A. Ashkenazi, S. Balasubramanian, B. Baller, C. Barnes, G. Barr, J. Barrow *et al.*, "Search for long-lived heavy neutral leptons and higgs portal scalars decaying in the MicroBooNE detector," *Physical Review D*, vol. 106, no. 9, p. 092006, 2022.

[8] E. D. Church, "Larsoft: A software package for liquid argon time projection drift chambers," 2014. [Online]. Available: https://arxiv.org/abs/1311.6774

[9] A. Smith, "Measurement of the muon-neutrino charged-current single charged-pion cross-section on argon with the MicroBooNE detector," Ph.D. dissertation, 2022. [Online]. Available: https://inspirehep.net/literature/2671418

[10] J. Esquivel, "The MicroBooNE experiment," in *AIP Conference Proceedings*, vol. 2109, no. 1. AIP Publishing, 2019.

[11] W. N. Cottingham and D. A. Greenwood, *An introduction to the standard model of particle physics*. Cambridge university press, 2007.

[12] M. K. Gaillard, P. D. Grannis, and F. J. Sciulli, "The standard model of particle physics," *Reviews of Modern Physics*, vol. 71, no. 2, p. S96, 1999.

[13] M. Spira, A. Djouadi, D. Graudenz, and R. Zerwas, "Higgs boson production at the lhc," *Nuclear Physics B*, vol. 453, no. 1-2, pp. 17–82, 1995.

[14] J. W. Valle, "Physics beyond the standard model," in *AIP Conference Proceedings*, vol. 359, no. 1. American Institute of Physics, 1996, pp. 42–146.

[15] P. Ramond, "Neutrinos: A glimpse beyond the standard model," *Nuclear Physics-Section B-PS-Proceedings Supplements*, vol. 77, pp. 3–12, 1999.

[16] G. Bellini, L. Ludhova, G. Ranucci, and F. Villante, "Neutrino oscillations," *Advances in High Energy Physics*, vol. 2014, no. 1, p. 191960, 2014.

[17] J. D. Lykken, "Beyond the standard model," *arXiv preprint arXiv:1005.1676*, 2010.

[18] L. Canetti, M. Drewes, and M. Shaposhnikov, "Matter and antimatter in the universe," *New Journal of Physics*, vol. 14, no. 9, p. 095012, 2012.

[19] D. Griffiths, *Introduction to elementary particles*. John Wiley & Sons, 2020.

[20] F. Reines and C. Cowan Jr, "Detection of the free neutrino," *Physical Review*, vol. 92, no. 3, p. 830, 1953.

[21] B. T. Cleveland, T. Daily, R. Davis Jr, J. R. Distel, K. Lande, C. Lee, P. S. Wildenhain, and J. Ullman, "Measurement of the solar electron neutrino flux with the homestake chlorine detector," *The Astrophysical Journal*, vol. 496, no. 1, p. 505, 1998.

[22] Y. Fukuda, T. Hayakawa, E. Ichihara, K. Inoue, K. Ishihara, H. Ishino, Y. Itow, T. Kajita, J. Kameda, S. Kasuga *et al.*, "Evidence for oscillation of atmospheric neutrinos," *Physical review letters*, vol. 81, no. 8, p. 1562, 1998.

[23] J. Boger, R. Hahn, J. Rowley, A. Carter, B. Hollebone, D. Kessler, I. Blevis, F. Dalnoki-Veress, A. DeKok, J. Farine *et al.*, "The sudbury neutrino observatory," *Nuclear Instruments and Methods in Physics Research Section A: Accelerators, Spectrometers, Detectors and Associated Equipment*, vol. 449, no. 1-2, pp. 172–207, 2000.

[24] M. Soderberg and M. Collaboration, "MicroBooNE: a new liquid argon time projection chamber experiment," in *AIP Conference Proceedings*, vol. 1189, no. 1. American Institute of Physics, 2009, pp. 83–87.

[25] P. A. Machado, O. Palamara, and D. W. Schmitz, "The short-baseline neutrino program at fermilab," *Annual Review of Nuclear and Particle Science*, vol. 69, no. 1, pp. 363–387, 2019.

[26] I. Gil-Botella, "The deep underground neutrino experiment (DUNE) program," *arXiv preprint arXiv:2412.14941*, 2024.

[27] F. Reines, "Neutrino interactions," *Annual Review of Nuclear Science*, vol. 10, no. 1, 1960.

[28] V. Papavassiliou, "Neutrino scattering studies in MicroBooNE," 2018. [Online]. Available: https://arxiv.org/abs/1810.05299

[29] H. Gallagher, G. Garvey, and G. Zeller, "Neutrino-nucleus interactions," *Annual Review of Nuclear and Particle Science*, vol. 61, no. 1, pp. 355–378, 2011.

[30] T. Golan, J. T. Sobczyk, and K. M. Graczyk, "Modeling nuclear effects in nuwro monte carlo neutrino event generator," Ph.D. dissertation, Ph. D thesis, University of Wroclaw, 2014.

[31] S. Dytman, "Final state interactions in neutrino-nucleus experiments." *Acta Physica Polonica B*, vol. 40, no. 9, 2009.

[32] A. M. Ankowski, A. Ashkenazi, S. Bacca, J. Barrow, M. Betancourt, A. Bodek, M. Christy, L. Doria, S. Dytman, A. Friedland *et al.*, "Electron scattering and neutrino physics," *Journal of Physics G: Nuclear and Particle Physics*, vol. 50, no. 12, p. 120501, 2023.

[33] M. Thomson, *Modern particle physics*. Cambridge University Press, 2013.

[34] C. Adams, M. Alrashed, R. An, J. Anthony, J. Asaadi, A. Ashkenazi, M. Auger, S. Balasubramanian, B. Baller, C. Barnes *et al.*, "First measurement of ν μ charged-current π 0 production on argon with the MicroBooNE detector," *Physical Review D*, vol. 99, no. 9, p. 091102, 2019.

[35] M. S. Athar and J. G. Morfin, "Neutrino (antineutrino)–nucleus interactions in the shallow-and deep-inelastic scattering regions," *Journal of Physics G: Nuclear and Particle Physics*, vol. 48, no. 3, p. 034001, 2021.

[36] Q. R. Ahmad, R. Allen, T. Andersen, J. Anglin, J. Barton, E. Beier, M. Bercovitch, J. Bigu, S. Biller, R. Black *et al.*, "Direct evidence for neutrino flavor transformation from neutral-current interactions in the sudbury neutrino observatory," *Physical review letters*, vol. 89, no. 1, p. 011301, 2002.

[37] H. Nunokawa, S. Parke, and J. W. Valle, "CP violation and neutrino oscillations," *Progress in Particle and Nuclear Physics*, vol. 60, no. 2, pp. 338–402, 2008.

[38] X. Qian and P. Vogel, "Neutrino mass hierarchy," *Progress in Particle and Nuclear Physics*, vol. 83, pp. 1–30, 2015.

[39] B. Dasgupta and J. Kopp, "Sterile neutrinos," *Physics Reports*, vol. 928, pp. 1–63, 2021.

[40] B. Fleming, "The MicroBooNE Technical Design Report." [Online]. Available: https://lss.fnal.gov/archive/design/fermilab-design-2012-04.pdf

[41] G. Karagiorgi, M. Collaboration *et al.*, "MicroBooNE: Searching for new physics in the neutrino sector with a 100-ton-scale liquid argon TPC," in *Journal of Physics: Conference Series*, vol. 375, no. 4. IOP Publishing, 2012, p. 042067.

[42] M. Mooney, "The MicroBooNE experiment and the impact of space charge effects," 2015. [Online]. Available: https://arxiv.org/abs/1511.01563

[43] J. L. Paton, "Towards an updated simulation of the booster neutrino beam," *arXiv preprint arXiv:2501.06323*, 2025.

[44] A. Abramov, N. Galyaev, V. Garkusha, J. Hylen, F. Novoskoltsev, A. Ryabov, and V. Zarucheisky, "Beam optics and target conceptual designs for the NuMI project," *Nuclear Instruments and Methods in Physics Research Section A: Accelerators, Spectrometers, Detectors and Associated Equipment*, vol. 485, no. 3, pp. 209–227, 2002.

[45] K. J. Kelly and P. A. Machado, "MicroBooNE experiment, NuMI absorber, and heavy neutral leptons," *Physical Review D*, vol. 104, no. 5, p. 055015, 2021.

[46] D. Crane, W. Freeman, M. Goodman, D. Johnson, A. Malensek, J. Morfin, S. O'Day, and J. Thomas, "Status report: Technical design of neutrino beams for the main injector (NuMI)," *Batavia, IL.: Fermilab Internal Report TM-1946*, 1995.

[47] P. Abratenko, J. Anthony, L. Arellano, J. Asaadi, A. Ashkenazi, S. Balasubramanian, B. Baller, C. Barnes, G. Barr, J. Barrow *et al.*, "Measurement of neutral current single π 0 production on argon with the MicroBooNE detector," *Physical Review D*, vol. 107, no. 1, p. 012004, 2023.

[48] B. Baller, "Liquid argon TPC signal formation, signal processing and reconstruction techniques," *Journal of Instrumentation*, vol. 12, no. 07, p. P07010, 2017.

[49] C. Adams, R. An, J. Anthony, J. Asaadi, M. Auger, L. Bagby, S. Balasubramanian, B. Baller, C. Barnes, G. Barr *et al.*, "Ionization electron signal processing in single phase LArTPCs. part i. algorithm description and quantitative evaluation with MicroBooNE simulation," *Journal of Instrumentation*, vol. 13, no. 07, p. P07006, 2018.

[50] C. Andreopoulos, C. Barry, S. Dytman, H. Gallagher, T. Golan, R. Hatcher, G. Perdue, and J. Yarba, "The GENIE neutrino monte carlo generator: physics and user manual," *arXiv preprint arXiv:1510.05494*, 2015.

[51] S. Agostinelli, J. Allison, K. a. Amako, J. Apostolakis, H. Araujo, P. Arce, M. Asai, D. Axen, S. Banerjee, G. Barrand *et al.*, "GEANT4—a simulation toolkit," *Nuclear instruments and methods in physics research section A: Accelerators, Spectrometers, Detectors and Associated Equipment*, vol. 506, no. 3, pp. 250–303, 2003.

[52] J. S. Marshall and M. A. Thomson, "The Pandora software development kit for pattern recognition," *The European Physical Journal C*, vol. 75, pp. 1–16, 2015.

[53] R. Acciarri, C. Adams, R. An, J. Anthony, J. Asaadi, M. Auger, L. Bagby, S. Balasubramanian, B. Baller, C. Barnes *et al.*, "The Pandora multi-algorithm approach to automated pattern recognition of cosmic-ray muon and neutrino events in the MicroBooNE detector," *The European Physical Journal C*, vol. 78, no. 1, pp. 1–25, 2018.

[54] A. Smith, "ubcc1pi technical note," https://www.hep.phy.cam.ac.uk/~asmith/ubcc1pi_technote.pdf, n.d., accessed: 2025-08-31.

[55] H.-J. Yang, B. P. Roe, and J. Zhu, "Studies of boosted decision trees for MiniBooNE particle identification," *Nuclear Instruments and Methods in Physics Research Section A: Accelerators, Spectrometers, Detectors and Associated Equipment*, vol. 555, no. 1–2, p. 370–385, Dec. 2005. [Online]. Available: http://dx.doi.org/10.1016/j.nima.2005.09.022